Chemical Engineering Journal 419 (2021) 129947

Contents lists available at ScienceDirect

Chemical Engineering Journal

journal homepage: www.elsevier.com/locate/cej

Dynamic flowsheet model development and digital design of continuous pharmaceutical manufacturing with dissolution modeling of the final product

Brigitta Nagy [a,b], Botond Szilágyi [c,*], András Domokos [a], Blanka Vészi [a], Kornélia Tacsi [a], Zsolt Rapi [a], Hajnalka Pataki [a], György Marosi [a], Zoltán K. Nagy [b,*], Zsombor Kristóf Nagy [a]

[a] Department of Organic Chemistry and Technology, Budapest University of Technology and Economics, H-1111 Budapest, Hungary
[b] Davidson School of Chemical Engineering, Purdue University, West Lafayette, IN 47907, USA
[c] Faculty of Chemical Technology and Biotechnology, Budapest University of Technology and Economics, H-1111 Budapest, Hungary

ARTICLE INFO

Keywords:
Dynamic flowsheet modeling
Integrated continuous manufacturing
Dissolution modeling
Sensitivity analysis
Optimization

ABSTRACT

The integration of continuous unit operations imposes a challenge on the pharmaceutical companies aspiring to achieve plant-wide continuous manufacturing due to the additional complexity of the dynamic interactions, process control and quality assurance. To overcome this challenge, flowsheet modeling emerged as a viable tool to gain deeper process knowledge. In this work, the dynamic model of the integrated continuous manufacturing of acetylsalicylic acid (ASA) was formed based on real continuous unit operations. Furthermore, the surrogate model of the *in vitro* dissolution test of ASA capsules was integrated into the flowsheet model the first time to analyze the integrated manufacturing in light of the dissolution specifications of an immediate-release formulation. Systematic optimization studies were performed on the integrated process and on the continuous unit operations step-by-step, which clearly revealed the impact of the plant-wide dynamic modeling, as the integrated approach resulted in the threefold increase in the overall productivity and the parallel decrease in the required reactant excess. Sensitivity analyses of the operating conditions and the kinetic parameters were also performed. The crystallization temperature emerged as one of the most critical parameters, which variation could even result in the failure of the dissolution specification. Moreover, by calculating the time-varying sensitivity indices, the dynamics of the error propagation could be studied. These results could facilitate the integration of existing continuous units, the development of the control strategy, and encourage the implementation of dissolution surrogate models into process flowsheet simulations.

1. Introduction

In the last decade, the pharmaceutical industry has started to undergo a vast transformation, which aims the implementation of flexible and efficient manufacturing as opposed to the traditional, conservative approach of fixed process conditions. This is promoted by several advances in parallel. From the technology point of view, innovations in continuous manufacturing equipment are rapidly emerging, providing options for consistent and economical production [1], and the regulatory agencies support the concept by providing guidelines [2] and initiatives, such the Quality-by-Design (QbD) [3] and Process Analytical Technology (PAT) [4]. These principles focus on the knowledge- and risk-based operation of the manufacturing process by the thorough mapping of the underlying critical material attributes (CMAs) and process parameters (CPPs) and their effect on the target product profile. The most important tools for this are real-time, in-line measurements as well as various statistical and mechanistic modeling methodologies [5,6].

Due to the additional complexity of continuous manufacturing lines, the importance of the systematic model-based design of the product and processes has increased. Mechanistic dynamic flowsheet models have been identified as excellent tools for representing the process knowledge and dynamically analyze the input–output relationship [7]. Together with widely used analysis tools, *e.g.,* sensitivity analysis [8], this contributes to the identification of the excessive variation and risk of error propagation, the optimization of the process, and the development of

* Corresponding authors: Davidson School of Chemical Engineering, Purdue University, West Lafayette, IN 47907, USA (Z.K. Nagy); Department of Organic Chemistry and Technology, Budapest University of Technology and Economics, H-1111 Budapest, Hungary (B. Szilagyi)
E-mail addresses: szilagyi.botond@vbk.bme.hu (B. Szilágyi), zknagy@purdue.edu (Z.K. Nagy).

https://doi.org/10.1016/j.cej.2021.129947
Received 10 December 2020; Received in revised form 16 March 2021; Accepted 17 April 2021
Available online 24 April 2021
1385-8947/© 2021 The Author(s). Published by Elsevier B.V. This is an open access article under the CC BY license (http://creativecommons.org/licenses/by/4.0/).

List of notations

A_i	Pre-exponential factor of the i^{th} reaction
AS	Antisolvent- solvent volume ratio
B	Nucleation rate [# $m^{-3}s^{-1}$]
b	Nucleation rate exponent [-]
c	Concentration in solution [M] (in synthesis); [kgm^{-3}] (in crystallization)
c_d	Mass fraction of API in the dissolution medium [-]
c_c^*	Equilibrium solubility in the crystallization [kgm^{-3}]
c_d^*	Equilibrium solubility in the dissolution medium [g ASA/ g solution]
c_i	Impurity concentration [M] (in the synthesis); [kgm^{-3}] (in crystallization)
c_{in}	Inlet concentration of solution [kgm^{-3}]
c_{norm}	Normalized concentration in solution [M] (in synthesis); [kgm^{-3}] (in crystallization)
c_s	Solid concentration [kgm^{-3}]
D	Dissolution rate [ms^{-1}]
D_R	Dissolved ratio [%]
d	Dissolution rate exponent [-]
$E(t)$	Residence time distribution
EE	Elementary effect
$E_{a,g}$	Growth activation energy [$Jmol^{-1}$]
$E_{a,i}$	Activation energy of the i^{th} reaction [$Jmol^{-1}$]
F	Flow rate [m^3s^{-1}]
G	Growth rate [ms^{-1}]
K_L	Langmuir constant [kgm^{-3}]
k_b	Nucleation rate coefficient [# m^{-3} s^{-1}]
k_d	Dissolution rate coefficient [m s^{-1}]
k_g	Growth rate coefficient [ms^{-1}]
k_i	Reaction rate constant of the i^{th} reaction [$Jmol^{-1}$]
k_v	Volume shape factor [-]
L	Linear size of crystals [m]
L_n	Nuclei size [m]
m_c	Sample mass in the dissolution test [kg]
N	Reactor number [#]
n	Population density [# m^{-4}]
n_{in}	Initial population density [#m^{-43}]
$nMSE$	Normalized mean square error [M^2]
$nMSE_{norm}$	Normalized mean square error calculated for normalized concentrations [M^2]
$O(D)$	Objective function
P	Purity [%]
p_i	Coefficients of size-dependent dissolution [-]
R	Universal gas constant, 8.314 $JK^{-1}mol^{-1}$
r_i	Rate law equation of the the i^{th} reaction
T	Temperature [°C]
t	Time [s]
V	Volume [m^3]
v	Antisolvent volume fraction in feed [-]
v_c	Crystal volume fraction in the dissolution medium [-]
X	Conversion [%]

Greek Letters

α	Effectiveness factor [-]
δ	Dirac-delta function
μ_2	2nd moment of the CSD [m^2m^{-3}]
μ_3	3rd moment of the CSD [m^3m^{-3}]
μ_M	Mean of elementary effects
ρ_c	Crystal density [kgm^{-3}]
ρ_d	Density of the dissolution medium [kgm^{-3}]
σ	Relative supersaturation [-]
σ^2	Standard deviation of the reactor residence time distribution [s]
σ_M^2	Standard deviation of elementary effects
τ	Mean residence time [s]

Subscripts

a	Acetylation
c	Crystallization
d	Dissolution
j	Sample point
m	Measured data
q	Quenching
X	Component in the reaction mixture
0	Initial state

control strategies [7,9]. Furthermore, when continuous communication is enabled between the model and the real process, a digital twin is created, which can be further used *e.g.,* for model-predictive control [10].

The concept of flowsheet modeling of continuous manufacturing has been already utilized by several authors for both the upstream (active pharmaceutical ingredient (API) manufacturing) and downstream (final product manufacturing) process steps, and software packages are also available to facilitate their development, such as gPROMS by Process Systems Enterprise [11]. As for the upstream part, a dynamic flowsheet model of ibuprofen synthesis and crystallization was developed and the uncertainty of the process was systematically studied [12]. Diab *et al.* studied the flowsheet model of the synthesis and crystallization of rufinamide [13] and nevirapine [14] in the view of techno-economic considerations, such as minimizing the production costs. Most recently, Icten *et al.* published a three-part series of papers [15–17] dealing with the development of a virtual plant for continuous manufacturing of carfilzomib intermediate, intending to gain a mechanistic understanding of the synthesis, crystallization and filtration unit operations, and to use the modeling framework to identify the CPPs that impact the conversion in their integrated system.

From the perspective of the downstream process modeling of solid products, mainly the continuous feeding, blending and tablet compression steps are integrated [18–20], but there are also examples for incorporating dry [21] and wet granulation [22] steps. Wang *et al.* [20] utilized the developed flowsheet model for the optimization of the process to minimize the total cost of the manufacturing. In most of the studies [18–20,22] sensitivity analysis was performed using the unit operation parameters (*e.g.,* residence times, flow rates) and final properties of the product, *e.g.,* tablet hardness and weight, API concentration as examined response variables. However, only a few modeling studies incorporated both the upstream and downstream manufacturing steps. Sen *et al.* [23,24] used such a model for analyzing the mixing properties in connection with the crystallization, filtration and drying processes, while in another study [25] the simulations were used to improve the overall productivity and quality of the manufacturing. Moreover, no

studies were found where the final quality of the formulation was assessed from the point of dissolution properties, although the *in vitro* dissolution is one of the most important and routinely analyzed quality attributes of solid pharmaceutical products [26]. Hence, the mathematical description could significantly contribute to the product and process development and release testing. This could be achieved either by first principles-based or black-box modeling approaches [27].

This paper presents the dynamic, integrated flowsheet model development for the continuous manufacturing of acetylsalicylic acid (ASA), involving a two-step flow synthesis and crystallization. The model was built to simulate the real continuous processes developed formerly by the authors of this paper [28,29]. In these former works, the unit operations were studied separately to analyze the effect of the different process parameters. As for the synthesis, the reaction mixture composition, processing temperature and residence times were optimized experimentally for maximal conversion and purity and minimal processing time [28], but the main priority was to obtain a reaction mixture which is directly connectable with electrospinning. The processing of this flow reaction mixture in continuous combined cooling and antisolvent crystallization process was also developed, where the effect of the crystallization temperature, the solvent system composition and residence time was studied on the crystal size distribution (CSD), yield and purity [29]. However, the integration of the synthesis and crystallization steps has not been achieved, yet. Therefore, to facilitate the integration of the existing unit operations, this work aimed the development of a dynamic flowsheet model to gain process understanding on the operation of the continuous, integrated process. This study is also the extension of a previous publication [30], where the dynamic model of the continuous crystallization was presented, but it dealt mainly with the integrated simulation of the continuous crystallization and filtration, *e.g.,* the effect on the CSD and solid concentration was analyzed on the continuous filtration. Consequently, together with the present work, the dynamic model of the fully continuous, integrated upstream process is achieved. The true potential of the integrated flowsheet model is demonstrated *via* optimization studies and sensitivity analysis. Furthermore, the surrogate *in vitro* dissolution model of capsules containing the obtained ASA powder is developed and integrated into the flowsheet model. Such a model can be useful when the dissolution of the capsules is affected solely by the API characteristics. Moreover, it could contribute to a better understanding of the CSD as CMA and the corresponding optimization and risk analysis of the API manufacturing process during the early stage of the drug development even in the case of more complex formulations. To the best of the authors' knowledge, this is the first time when flowsheet modeling is utilized for studying the dissolution properties of the final product of continuous pharmaceutical manufacturing.

2. Materials and methods

2.1. Experimental procedures

The mathematical model of the integrated continuous synthesis-crystallization process and the *in vitro* dissolution properties was developed based on real, laboratory-scale continuous processes and experimental data. The synthesis and crystallization procedures have been originally published in [28] and [29] and the experiments used for the parameter estimation and validation of the synthesis and crystallization steps came from these works. Although the experiments were originally conducted for the experimental development of the technologies and not for the purpose of the mathematical model fitting, they were found to be suitable for the parameter estimations as the viable ranges of the operating conditions were explored in different combinations. The experiments were divided into calibration and validation sets. A quasi-random division was aimed: the ratio depended on the total number of the available experiments, and the validation experiments were selected randomly, but it was also accounted that the validation set should cover the whole range of the settings.

2.1.1. Synthesis

The modeling of the continuous synthesis of ASA was based on the experimental work of Balogh *et al.* [28]. The two-step flow synthesis consisted of acetylation and a subsequent quenching step. For acetylation, a 1 mol L^{-1} solution of salicylic acid (SA) was prepared in ethyl acetate (EtOAc), also containing phosphoric acid (H_3PO_4) as a catalyst in 0.1 mol equivalent relative to SA. SA was acetylated continuously with excess acetic anhydride (AA). In the subsequent quenching step ethanol (EtOH) was added to the reaction mixture of the first step, to remove the excess AA and the quenchable impurities. The reactions were carried out in 8.77 and 1.83 m long tube flow reactors for the acetylation and quenching step, respectively with an inner diameter of 0.787 mm. 4 bar was used to maintain constant fluid flow conditions.

Acetylation experiments were conducted first in batch mode to analyze the effect of the AA excess (AA_{eq}, mole equivalent relative to SA) and the acetylation temperature (T_a), then in continuous mode to adjust the temperature and the residence time (τ_a), while AA_{eq} was fixed to 5, based on the outcomes of the batch experiments. At the quenching step, the EtOH ratio ($EtOH_{eq}$, mole equivalent relative to the initial SA), residence time (τ_q), and quenching temperature (T_q), were analyzed in continuous mode, whereas AA_{eq}, T_a and τ_a were fixed to 5, 55 °C and 180 min, respectively. The composition of the reaction mixture was measured by HPLC [28] every 10–20 min in the case of the batch acetylation and in the steady state of the continuous runs. Tables 1 and 2 summarize the acetylation and quenching experimental settings utilized in this study to estimate the kinetic parameters of the mathematical model. For further details on the experimental setup, the reader is referred to [28].

2.1.2. Crystallization

A combined cooling and antisolvent (CCAS) continuous crystallization method has been developed to crystallize the ASA from the reaction mixture obtained in the flow synthesis [29]. The crystallization experiments were performed in mixed-suspension, mixed-product-removal (MSMPR) continuous crystallizer operated at 235 mL constant volume and using heptane as antisolvent. Experiments were performed with 0.8 antisolvent volume fraction (v) and varying flow rates (F_c), temperatures (T_c) and residence times (τ_c) in the ranges of 5–20 mL min^{-1}, 2–25 °C and 10–50 min, respectively. Details on the crystallization experimental setup, procedure, the experiments for the kinetic parameter estimation and the parameter estimation can be found in our previous publications [29,30].

2.1.3. In vitro dissolution testing

To investigate the effect of the crystal size distribution (CSD) on the *in vitro* dissolution of the final product (*e.g.,* capsule), samples for dissolution testing were prepared by sieving ASA powder using 63, 100,

Table 1
Experimental setting used for the kinetic parameter estimation and validation of the acetylation step.

Experiment No.	T_a [°C]	AA_{eq} [-]	Experiment No.	T_a [°C]	τ_a [min]
A_{batch} **1**	20	1.5	$A_{cont.}$ **1**	50	60
A_{batch} **2**	20	5	$A_{cont.}$ **2**	50	120
A_{batch} **3**	50	1.5	$A_{cont.}$ **3**	70	120
A_{batch} **4**	50	10	$A_{cont.}$ **4**	60	90
A_{batch} **5**	77	5	$A_{cont.}$ **5**	65	180
A_{batch} **6**	77	10	$A_{cont.}$ **6**	45	120
A_{batch} **Val 1**	20	10	$A_{cont.}$ **7**	65	120
A_{batch} **Val 2**	50	5	$A_{cont.}$ **8**	55	150
A_{batch} **Val 3**	77	1.5	$A_{cont.}$ **9**	55	180
			$A_{cont.}$ **Val 1**	70	60
			$A_{cont.}$ **Val 2**	60	90
			$A_{cont.}$ **Val 3**	45	180

Table 2
Experimental setting used for the kinetic parameter estimation and validation of the quenching step.

Experiment No.	T_q [°C]	τ_q [min]	$EtOH_{eq}$ [-]	Experiment No.	T_q [°C]	τ_q [min]	$EtOH_{eq}$ [-]
Q 1	80	15	3	***Q 11***	80	21	3
Q 2	80	5	6	***Q 12***	90	26	3
Q 3	60	15	6	***Q 13***	100	31	3
Q 4	60	15	3	***Q Val 1***	80	15	6
Q 5	60	5	6	***Q Val 2***	80	5	3
Q 6	70	10	4.5	***Q Val 3***	60	5	3
Q 7	85	22	3	***Q Val 4***	70	10	4.5
Q 8	95	29.5	3	***Q Val 5***	90	26	3
Q 9	100	33	3	***Q Val 6***	100	21	3
Q 10	80	31	3				

150, 200, 300 and 500 μm sieve openings as well as by combining equal weights of sieve fractions (Table 3). Additionally, two continuously crystallized crystal products (MSMPR 1 and 2) were also used for validation. The CSD of each sample was collected by a Parsum IPP 70-s inline particle sizing probe (Malvern Panalytical Ltd., UK) in batch mode. The samples were dispersed into the instrument for estimating the cord length of the crystals, which were used to construct the number-based CSDs in the 50–2000 μm size range with a logarithmic grid with 50 bins.

Then dissolution tests of 100 mg powders were carried out in powder form as well as in some cases (see Table 3) filling them into capsules. The tests were performed in a Hanson SR8-Plus dissolution tester (Hanson Research, USA) using the paddle method (United States Pharmacopoeia II). In the case of the capsules, a spiral capsule sinker was used to prevent the floating of the capsules. 900 mL of 0.1 N HCl solution was used as dissolution medium, stirred at 100 rpm and kept at constant temperature of 37 ± 0.5 °C, which ensured sink condition. An on-line coupled Agilent 8453 UV–VIS spectrophotometer (Hewlett-Packard, USA) was used to measure the concentration of dissolved ASA for 2 h by sampling every 2.5 min until 20 min, followed by sampling in every 10 min until 120 min.

Due to the possible degradation of the dissolved ASA to SA during the dissolution process (in preliminary tests ~ 2% of the ASA degraded in 1 h), the SA and ASA needed to be quantified simultaneously. Although this would be possible by an HPLC method, a Partial Least Squares (PLS) calibration model was developed for the evaluation of the UV–VIS spectra based on HPLC data to avoid the lengthy and labor-intensive HPLC measurement. The degradation was observed in the UV–VIS spectra by the gradual shift of the 229 nm ASA band, the appearance of a weak and broad SA band in the 270–320 nm region, which overlapped with a weak signal of the ASA in the 260–280 nm region. Therefore, the PLS model was developed for the 278–320 nm region of the mean-centered UV absorbance spectra with 2 latent variables. The calibration samples contained different amounts of ASA and SA in the 80–120 and 0–30 mg L^{-1} concentration ranges, respectively, which composition was determined by an HPLC method [28]. The R^2 of the calibration and cross-validation was both 0.98, while a root mean square error of calibration and cross-validation of 4.78 and 5.46 mg L^{-1} was obtained, respectively.

Table 3
Calibration and validation samples of the *in vitro* dissolution studies. The samples that were measured both in powder and capsule form are indicated in bold.

Calibration samples		Validation samples	
Sample name	**Sieve fraction [μm]**	**Sample name**	**Sieve fraction [μm]**
63	**63–100**	**63 + 300**	**(63–100) +(300–500)**
100	**100–150**	**63 + 100 + 150**	**(63–100) +(100–150) +(150–200)**
150	**150–200**	63 + 200 + 500	(63–100) +(200–300)+ (>500)
200	**200–300**	0 + 63	(<63)+(63–100)
300	**300–500**	**100**	**100–150**
500	**>500**	**150**	**150–200**
100 + 300	**(100–150) +(300–500)**	**200**	**200–300**
150 + 200	**(150–200) +(200–300)**	300	300–500
200 + 300 + 500	**(200–300) +(300–500) +(>500)**	MSMPR 1	–
63 + 500	**(63–100) +(>500)**	MSMPR 2	–

2.2. Mathematical modeling and kinetic parameter identification

The model-equations were solved in MATLAB R2020a (MathWorks®, USA), the integrated flowsheet simulation was implemented in Simulink 10.1 (MathWorks®, USA).

2.2.1. Flow synthesis

Based on the experimental observations [28], the reaction network of the acetylation step was constructed by accounting not only the conversion of SA to ASA (Eq. (1.a)) but also the formation of two impurities, namely acetylsalicylic ethanoic anhydride (Impurity A) and acetylsalicylic anhydride (Impurity B) [28] (Eqs. (1.b) -(1.d)).

$$SA + AA \xrightarrow{k_1} ASA + HA \tag{1.a}$$

$$ASA + AA \xrightarrow{k_2} A + HA \tag{1.b}$$

$$A + ASA \overset{k_3, k_{3r}}{\rightleftharpoons} B + HA \tag{1.c}$$

$$SA + 2AA \xrightarrow{k_4} A + 2HA \tag{1.d}$$

where *HA*, *A* and *B* denote acetic acid, Impurity A and Impurity B, respectively.

At the subsequent quenching step, it was observed, that besides the decomposition of AA using EtOH, possible reactions of Impurity A and ASA also have to be considered (Eqs. (2.a) -(2.c)):

$$A + EtOH \xrightarrow{k_5} ASA + EtOAc \tag{2.a}$$

$$AA + EtOH \xrightarrow{k_6} EtOAc + HA \tag{2.b}$$

$$ASA + EtOH \overset{k_7, k_{7r}}{\rightleftharpoons} SA + EtOAc \tag{2.c}$$

In Eqs. (1)-(2) k_i corresponds to the reaction rate constant expressed as

$$k_i = A_i \cdot e^{-\frac{E_{a,i}}{RT}} \tag{3}$$

where A_i is the pre-exponential factor, $E_{a,i}$ [J mol^{-1}] is the activation energy, T [°C] is the reaction temperature and R is the gas constant (8.314 J K^{-1} mol^{-1}) of the i^{th} reaction.

The rate law equations were expressed as

$$r_i = k_i \cdot \prod c_X(t) \tag{4}$$

where c_X denotes the concentration of the reaction component taking part in the given reaction. The rate law equations for each reaction are detailed in the Appendix.

The continuous flow synthesis can be described using an axial dispersion tubular reactor model, which consists of a set of partial differential equations (PDEs) [31]:

$$\frac{\partial c_X}{\partial t} = -v_x \cdot \frac{\partial c_X}{\partial x} + D_m \cdot \frac{\partial^2 c_X}{\partial x^2} + r \tag{5}$$

where x corresponds to the spatial coordinate along the flow reactor, t is the time, c_X is the concentration of the reaction component X, D_m is dispersion coefficient and r represents a set of rate law equations. The initial conditions for the PDEs correspond to the initial concentrations along the length of the reactor. At the reactor inlet and outlet, the Danckwerts boundary conditions apply [31], where the inlet boundary conditions are

$$v_x \cdot [c_X(0) - c_{X0}] - D_m \cdot \left.\frac{dc_X}{dx}\right|_{x=0} = 0 \tag{6}$$

and the outlet boundary conditions are given as:

$$\left.\frac{dc_X}{dx}\right|_{x=L} = 0 \tag{7}$$

Although Eqs. (5)-(7) enables the concentration calculation through time and the spatial coordinate of the reactor, it requires the solution of PDEs, which cannot be directly implemented in the integrated, dynamic flowsheet simulation in Simulink. To overcome this problem, a tank-in-series (TIS) approximation of the axial dispersion model was used in this study, approximating the tubular flow reactor as a cascade of N equal-sized continuous stirred-tank reactors (CSTRs). In this case, assuming constant working volume, an ordinary differential equation (ODE) system was formed for each CSTR to describe the changes in the concentrations of the reaction components for both the acetylation (Eq.8) and quenching (Eq.9) steps. (See the Appendix for the complete ODE systems.)

$$\frac{dc_{a,X}}{dt} = r + \frac{c^0_{a,X} - c_{a,X}}{\tau_a} \tag{8}$$

$$\frac{dc_{q,X}}{dt} = r + \frac{c^0_{q,X} - c_{q,X}}{\tau_a} \tag{9}$$

In Eqs. (8)-(9), the subscripts a and q are referring to the acetylation and quenching step, respectively, τ denotes the mean residence time [s] in the reactor, which is infinite during the modeling of the batch reactions and expressed as Eq. (10) for the continuous reactor.

$$\tau = \frac{V}{F} \tag{10}$$

where V is the reactor volume [m^3] and F is the flow rate [$m^3\ s^{-1}$]. For Eqs. (8)-(9), the initial conditions $c_{a,X}(0) = c_{a,X,0}$ and $c_{q,X}(0) = c_{q,X,0}$ apply, where the initial $c_{a,X,0}$ concentration was calculated based on the concentration of the SA solution and the applied AA_{eq}, while $c_{q,X,0}$ was calculated from the outlet acetylation concentrations and $EtOH_{eq}$.

The volume of the CSTRs in the cascade (V_i) is calculated by dividing the total volume of the flow reactor by the reactor number N (Eq. (11)).

$$V_i = \frac{V}{N} \tag{11}$$

The number of the necessary reactors was derived based on the reactor residence time distribution (RTD). The reactors were assumed to operate as laminar flow reactors (the Reynolds numbers ranged from 0.5 to 5 for the reactor settings summarized in Table 1-2), which residence time is expressed as Eq. (12) [31].

$$E(t) = \begin{cases} 0 \ if \ t < \dfrac{\tau}{2} \\ \dfrac{\tau^2}{2t^3} if \ t \geq \dfrac{\tau}{2} \end{cases} \tag{12}$$

where the mean residence time (τ) and the standard deviation (σ^2) of the RTD is calculated as:

$$\tau = \int_0^\infty tE(t)dt \tag{13}$$

$$\sigma^2 = \int_0^\infty (t-\tau)^2 E(t)dt \tag{14}$$

The number of necessary reactors is then obtained as:

$$N = \frac{\sigma^2}{\tau^2} \tag{15}$$

N was calculated for the τ_a and τ_q values detailed in Tables 1 and 2. The calculations resulted in N values between 3.920 and 3.933, with a slight rising trend as τ increased. Therefore, 4 CSTRs were used in cascade for the simulation of both the acetylation and quenching steps in the continuous reactors. The compartmental model assumes that there is only convective transfer between the CSTRs of the cascade without diffusive transfer, which is a basic assumption of the traditional tank-in-series model, as detailed in [31].

The reaction kinetic parameters (A_i and $E_{a,i}$) were estimated using the batch and the continuous experimental data for the acetylation step in different combinations and the flow reactions for the quenching step (see Tables 1 and 2). The calculations were performed using the Covariance Matrix Adaptation Evolution Strategy (CMA-ES), an accelerated global optimization algorithm that improves the chance of finding the global optimum [32]. The objective functions were formed depending on whether the batch or the continuous experimental data was used for parameter estimation. In the case of the batch data, the normalized mean square errors (nMSE) were calculated between the calculated and measured concentrations for SA, ASA, Impurity A and Impurity B. Normalization of the error components was performed by the difference between the maximum and minimum of the concentration for each component, so that each error component had equal weight in the objective function, irrespective of its concentration range (Eq. (16)).

$$nMSE_X = \frac{\frac{1}{K}\sum_{j=1}^{K}\left(c_{j,X} - c_{m,j,X}\right)^2}{\max\left(c_{m,X}\right) - \min\left(c_{m,X}\right)} \tag{16}$$

where $c_{m,j}$ and c_j are the measured and calculated concentrations in the j^{th} sample point, K is to the total number of the sample points and X denotes component SA, ASA, Impurity A and Impurity B. For the continuous experiments, only steady state concentrations were available, from which the nMSEs were further calculated by using normalized concentration values ($c_{norm,m,j}$, $c_{norm,j}$), where the normalization was done to unit sum (Eq. (17)). This could be reasoned by the fact, that for the simulation of the continuous integrated processes, it is more important to capture the concentrations relative to each other caused by the varying operation parameters, rather than the absolute concentrations. In this way, information on the absolute concentration is eliminated, but including the $nMSE_{norm,X}$ terms into the objective function (Eq. (21)) guided the parameter estimation to retain the concentrations relative to the different settings.

$$nMSE_{norm,X} = \frac{\frac{1}{K}\sum_{j=1}^{K}\left(c_{norm,j,X} - c_{norm,m,j,X}\right)^2}{\max\left(c_{norm,m,X}\right) - \min\left(c_{norm,m,X}\right)} \tag{17}$$

Table 4
Constants and kinetic parameters of the crystallization model.

Variable	Unit	Value
k_v	–	$\pi/6$
ρ_c	kgm^{-3}	1400
V_c	m^3	2.35×10^{-4}
k_b	$\#\ m^{-3}s^{-1}$	3.48×10^{6}
b	–	0.928
k_g	ms^{-1}	8.51×10^{11}
$E_{a,g}$	$Jmol^{-1}$	97,323

Table 5
Constants of the *in vitro* dissolution model.

Variable	Unit	Value
m_c	mg	100
V_d	mL	900
ρ_d	kg m^{-3}	1000
$t_{d,max}$	min	120
T_d	°C	37
c_d^*	[g ASA/g solution]	3.98×10^{-3}

where

$$c_{norm,j,X} = \frac{c_{j,X}}{\sum_{j=1}^{K} c_{j,X}} \tag{18}$$

$$c_{norm,m,j,X} = \frac{c_{m,j,X}}{\sum_{j=1}^{K} c_{m,j,X}} \tag{19}$$

Denoting the vector of the considered decision variables by D, the objective functions of the parameter estimation (O) from batch and continuous data took the form:

$$O(D)_{batch} = nMSE_{SA} + nMSE_{ASA} + nMSE_A + nMSE_B \tag{20}$$

$$O(D)_{cont} = nMSE_{SA} + nMSE_{ASA} + nMSE_A + nMSE_B + w\cdot\left(nMSE_{norm,SA} + nMSE_{norm,ASA} + nMSE_{norm,A} + nMSE_{norm,B}\right) \tag{21}$$

In Eq. (20)-(21), the decision variable D comprises the A_i and $E_{a,i}$ parameters of the acetylation and quenching reactions (see Table 6 and 7). In Eq. (21), the weight factor (w) was set to 2 based on preliminary optimizations such as both the absolute concentration values as well as their relative changes through the experiments were satisfactory. When both the batch and continuous data were used for parameter estimation, the objective function was obtained by summarizing $O(D)_{batch}$ and $O(D)_{cont}$. The error of fit to the validation experiments was calculated the same way, with the exception that for the continuous samples $w = 0$ were used for a better comparison of the batch and continuous results. In addition to the estimation of nominal parameters, the effects of parameter uncertainties were analyzed on the simulated outputs. This was performed by executing a sufficiently large number of simulations (1000) with kinetic parameter combinations, obtained by Monte-Carlo sampling from the confidence hyper ellipsoid defined by the covariance matrix of the nominal parameters [33].

Table 7
Estimated kinetic parameters and validation errors for the quenching and dissolution models (95% confidence intervals are in parenthesis).

Quenching		**Dissolution**	
A_5	**1.44** $\times$ **10^5**(1.15 $\times$ 10^5; 1.82 $\times$ 10^5)	k_d	**1.98** $\times$ **10^{-7}**(3.14 $\times$ 10^{-7}; 1.25 $\times$ 10^{-7})
$E_{a,5}$	**55,595** (fix)	d	**0** (fix)
A_6	**0** (fix)	p_1	**1** (fix)
$E_{a,6}$	**0** (fix)	p_2	**0** (fix)
A_7	**1.49** $\times$ **10^7**(9.19 $\times$ 10^6; 2.41 $\times$ 10^7)	*Error*	**68.73**
$E_{a,7}$	**84,153** (fix)		
$A_{,r7}$	**8.22** $\times$ **10^1**(8.27 $\times$ 10^0; 8.17 $\times$ 10^2)		
$E_{a,r7}$	**45,883** (fix)		
Error	**1.90**(1.57; 2.35)		

2.2.2. Continuous crystallization

The continuous crystallization of ASA from the reaction mixture was simulated using a one-dimensional population balance model (PBM), developed formerly by the authors of this paper [30]. It was assumed that the kinetics does not depend on the solvent composition. In the previous study [30], various model structures were tested, accounting secondary nucleation, size-independent growth and size-independent agglomeration and it was observed that neglecting agglomeration did not result in considerable performance degradation: the model with agglomeration resulted in 0.770 fitting error as opposed to the 0.772 error obtained without agglomeration, and no visible difference could be observed in the fit of the validation CSDs. For more details see [30]. Since the simulation of agglomeration has the highest computational burden amongst the considered mechanisms, a secondary nucleation and growth PBM was applied. In this way, the PB equation (PBE) took the form of Eq. (22), where the first term on the left-hand side defines

Table 6
Estimated kinetic parameters and validation errors for the acetylation with different model structures (95% confidence intervals are in parenthesis).

	Model 1	***Model 2***	***Model 3***	***Model 4***
Dataset	**batch**	**Batch**	**continuous**	**batch+continuous**
Reaction schemes	Eqs. (1.a, 1.b, 1.c)	Eqs. (1.a, 1.c, 1.d)	Eqs. (1.a, 1.c (irreversible), 1.d)	Eqs. (1.a, 1.c, 1.d)
A_1	**6.06** $\times$ **10^5**(3.77 $\times$ 10^4; 9.76 $\times$ 10^6)	**4.34** $\times$ **10^2**(6.46 $\times$ 10^1; 2.91 $\times$ 10^3)	**8.93** $\times$ **10^3**(1.23 $\times$ 10^3; 6.46 $\times$ 10^4)	**7.48** $\times$ **10^2**(3.28 $\times$ 10^2; 1.71 $\times$ 10^3)
$E_{a,1}$	**56,313**(49383; 63244)	**38,802**(34017; 43587)	**48,138**(42684; 53592)	**40,172**(38072; 42273)
A_2	**1.93** (6.31 $\times$ 10^{-2}; 5.59 $\times$ 10^1)	**0** (fix)	**0** (fix)	**0** (fix)
$E_{a,2}$	**28,350**(19283; 37417)	**0** (fix)	**0** (fix)	**0** (fix)
A_3	**3.54** $\times$ **10^{16}**(6.06 $\times$ 10^{14}; 2.07 $\times$ 10^{17})	**2.83** $\times$ **10^6**(6.79 $\times$ 10^4; 1.18 $\times$ 10^8)	**6.28** $\times$ **10^6**(3.94 $\times$ 10^{-2}; 9.99 $\times$ 10^{14})	**1.38** $\times$ **10^8**(3.60 $\times$ 10^{-9}; 5.28 $\times$ 10^{24})
$E_{a,3}$	**124,397**(112501; 136294)	**62,468**(52756; 72180)	**74,964**(20396; 129533)	**70,497**(-33965; 174960)
A_{r3}	**3.17** $\times$ **10^{-14}**(6.74 $\times$ 10^3; 1.49 $\times$ 10^{-5})	**4.70** $\times$ **10^{-4}**(2.31 $\times$ 10^{-2}; 9.58 $\times$ 10^{-6})	**0** (fix)	**1.59** $\times$ **10^3**(8.72 $\times$ 10^{-2}; 2.89 $\times$ 10^{-5})
$E_{a,r3}$	**0** (fix)	**0** (fix)	**0** (fix)	0 (fix)
A_4	**0** (fix)	**2.23** $\times$ **10^4**(2.34 $\times$ 10^3; 2.12 $\times$ 10^5)	**2.53** $\times$ **10^4**(1.72 $\times$ 10^3; 3.71 $\times$ 10^5)	**6.46** $\times$ **10^4**(5.02 $\times$ 10^3; 8.32 $\times$ 10^5)
$E_{a,4}$	**0** (fix)	**53,862**(48025; 59700)	**56,114**(49473; 62755)	**56,601**(49975; 63228)
$Error_b$	**1.36**(0.63; 2.29)	**0.79**(0.41; 1.70)	**0.86**(0.17; 2.78)	**1.02**(0.48; 2.15)
$Error_c$	**95.0**(73.7; 113.1)	**35.4**(19.3; 57.6)	**46.8**(11.8; 97.6)	**42.5**(23.2; 71.4)

the temporal evolution of the crystal's population density function ($n(L,t)$, denoting the number of crystals in the L,$L+dL$ crystal size domain at t time) and the second term takes into account the effect of crystal growth. The right-hand side stands for the nucleation and the in- and outflow of the continuous system, respectively.

$$\frac{\partial n(L,t)}{\partial t} + G\frac{\partial n(L,t)}{\partial L} = B\delta(L-L_n) + \frac{n_{in}(L,t)}{\tau_c} - \frac{n(L,t)}{\tau_c} \tag{22}$$

In Eqs. (22), L denotes the crystal size [m], t is the time [s], G is the rate of crystal growth [m s^{-1}], B is the rate of nucleation [#m^{-3} s^{-1}], $n_{in}(L,t)$ is the number density function of crystals in the feeding stream [#m^{-4}], τ_c is the mean residence time in the crystallizer [s], L_n is the nuclei size [m] and δ is the Dirac-delta function. L_n has a very small, practically zero value, therefore it was neglected in the calculations.

The initial condition (Eq. (23)) of the PBE gives the initial CSD $n_0(L)$ in the crystallizer, whereas the boundary condition states that the crystals have a finite size (Eq. (24)).

$$n(L,0) = n_0(L) \tag{23}$$

$$n(L\to\infty,t) = 0 \tag{24}$$

The secondary nucleation (Eq. (25)) is expressed as the function of the second moment of the distribution (μ_2 [m^2 m^{-3}], (Eq.(27)) and the relative supersaturation (σ_c) [-] (Eq.(27)).

$$B(\sigma_c,\mu_2) = k_b\sigma_c^b\mu_2 \tag{25}$$

$$\mu_2 = \int_0^\infty L^2 n(L,t)dL \tag{26}$$

$$\sigma_c = \frac{c_c}{c_c^*} - 1 \tag{27}$$

In Eqs. (25)-(27), k_b and b denote the nucleation rate coefficient [# m^{-3} s^{-1}] and the nucleation rate exponent [-], respectively. c_c^* is the solubility [kg m^{-3}], which, in the case of a combined cooling-antisolvent crystallization, is dependent on the crystallization temperature (T_c [°C]) and the antisolvent volume fraction v [-] [30]:

$$c^*(T_c,v) = 54.51 - 118.1v + 69.55v^2 + 2.078T_c - 2.459vT_c \tag{28}$$

The growth rate is described as a function of the relative supersaturation and a temperature-dependent rate factor ($G_0(\sigma,T_c)$), as expressed in Eq. (29), where k_g denotes the growth rate coefficient [m s^{-1}], $E_{a,g}$ represents the activation energy of growth [J mol^{-1}].

$$G_0(\sigma_c,T_c) = k_g\sigma_c\exp\left(\frac{-E_{a,g}}{RT_c}\right) \tag{29}$$

Along with the PBE, the corresponding mass balances were solved for the solute concentration (Eq. (30)) and antisolvent volume fraction (Eq. (31)).

$$\frac{dc_c}{dt} = -\rho_c k_v\left(BL_n^3 + 3G_0\int_0^{L_{max}} L^2 n(L,t)dL\right) + \frac{c_{in,c}-c_c}{\tau_c} \tag{30}$$

$$\frac{dv}{dt} = \frac{v_{in}-v}{\tau_c} \tag{31}$$

where ρ_c [kg m^{-3}] and k_v [-] represent the crystal density and volumetric shape factor, respectively. The mass balances have the $c(0) = c_0$ and $v(0) = v_0$ initial conditions, which give the initial solute concentration and solvent composition in the crystallizer.

A semi-discrete implementation of a high-resolution finite volume method (HR-FVM) was applied to solve the growth part (convective flux) of the PBE [34], simulating the CSD in the range of 0–2000 μm on a uniform grid with 500 cells. The constants used for the simulations are summarized in Table 4. For further details about the crystallization model development, the reader is referred to [30].

2.2.3. In vitro dissolution prediction

The *in vitro* dissolution of the obtained ASA crystals was described using a population balance model. It could be assumed, that in the USP apparatus the temporal evolution of the $n(L,t)$ population density function (*i.e.,* the number-based CSD) is only affected by the dissolution of the particles. Therefore, the PBE takes the form of

$$\frac{\partial n(L,t)}{\partial t} - D\frac{\partial n(L,t)}{\partial L} = 0 \tag{32}$$

where D is the rate of the dissolution [m s^{-1}] and the same initial and boundary conditions (Eq. (23–24)) apply as for the crystallization PBM. The calculation of the initial population density [# m^{-4}] from the normalized (measured or simulated) CSD is summarized in the Appendix.

The size-dependent dissolution rate is defined as

$$D(\sigma_d,L) = k_d\sigma_d^d(1+p_1L)^{p_2} \tag{33}$$

where k_d and d denote the dissolution rate coefficient [m s^{-1}] and the dissolution rate exponent [-] and p_1 and p_2 are coefficients indicating the size-dependence of the dissolution. σ_d is the relative supersaturation, expressed in the same manner as for the crystallization model (Eq. (27)). Based on literature data [35,36], the solubility of ASA (c_d^*) in the 0.1 N HCl dissolution medium was approximated as 4 mg mL^{-1}, which was further converted to mass fractions. As the dissolution tests were conducted by dissolving 100 mg ASA in the 900 mL dissolution medium (*i.e.,* the maximum concentration is 0.11 mg mL^{-1}), this means, that experimentally the sink condition criteria met (*i.e.,* dissolution media can dissolve at least 3 times the amount of drug that is the dosage form). Nevertheless, the supersaturation was accounted in Eq. (33) for the sake of better generalization of the model but is not expected to have a significant effect in the studied case. As the dissolution tester maintains a constant dissolution temperature (T_d) of 37 °C, the temperature dependence solubility is neglected.

Along with the PBE, the mass balance for the solute concentration was formulated as Eq. (34), with the initial condition of $c(0) = 0$.

$$\frac{dc_d}{dt} = 3\rho_c k_v\int_0^\infty D(\sigma_d,L)L^2 n(L,t)dL \tag{34}$$

where c_d denotes the ASA concentration in the dissolution medium. From Eq. (34), the dissolution curve was obtained as

$$D_R(t) = \frac{c_d(t)(m_c+\rho_d V_d)}{m_c}\cdot 100 \tag{35}$$

where m_c, V_d and ρ_d correspond to the sample mass [kg], the volume of the dissolution medium [m^3] and the density of the dissolution medium [kg m^{-3}]. The values of these parameters were chosen based on the experimental method (see Section 2.1.3) and summarized in Table 5. D_R [%] is the dissolved ratio, expressed as the percentage of the total sampled mass. Corresponding to the experiments, the dissolution was modeled for $t_{d,max} = 120$ min and during the integrated simulation the time (T85) needed to reach the 85% D_R was also calculated.

Similar to the crystallization model, a semi-discrete implementation of a high-resolution finite volume method (HR-FVM) was used for solving the PBE using the same computational grid. The parameter estimation was performed using the calibration powder samples summarized in Table 3 and using the root mean square error (RMSE) between the measured and calculated concentration values as an objective function ($O(k_d,d,p_1,p_2)_d$).

$$O(k_d,d,p_1,p_2)_d = \sqrt{\frac{\sum_{j=1}^{K_d}\left(D_{R,j}-D_{R,m,j}\right)^2}{K_d}} \tag{36}$$

where $D_{R,m,j}$ and K_d denote the measured dissolved ratio and the total number of the sampled time points, respectively.

For the sake of simplicity in the integrated simulation, it was

assumed, that the dissolution of the ASA capsules is mainly affected by the varying ASA particle sizes, that is the presence of the capsule shell causes a constant retarding effect. This assumption was also supported by the measured dissolution curves (see Section 3.1). Therefore, the model for the dissolution of the capsules was modified only by considering a linear relationship between the powder dissolution rate ($D(\sigma_d, L)$), that is multiplying $D(\sigma_d, L)$ with a constant retarding factor. Once $D(\sigma_d, L)$ was determined based on the powder dataset, the retarding factor was also estimated based on the experimental capsule dissolution curves (by minimizing the difference between the measured and simulated curves). Further, more detailed studies will be conducted in the future when the relationship between the powder and capsule dissolution is more complex, *e.g.,* when considerable lag time also need to be accounted in the model due to the presence of the capsule shell, or the effect of excipients also need to be accounted.

2.2.4. Integrated flowsheet model

After developing the mathematical models of the unit operations as described in Section 2.2.1-2.2.3., the integrated process model was constructed as illustrated in Fig. 1. The properties of the reaction mixture were calculated by the synthesis model. The flow rate after quenching (F_q) is used for calculating the necessary flow rate of the antisolvent to obtain the defined antisolvent-solvent volume fraction (v). For simplicity, the antisolvent-solvent volume ratio (AS) is used further as an operating parameter, from where v is obtained as

$$v = \frac{AS}{AS+1} \tag{37}$$

and consequently, the flow rate in the crystallizer is calculated:

$$F_c = 76F_q + 76F_q \cdot AS \tag{38}$$

As can be seen in Section 2.1, the synthesis and the crystallization experiments were conducted at a different scale, being the volume of the acetylation and quenching tube 4.19 and 0.89 mL, respectively, compared to the 235 mL MSMPR working volume. Therefore, F_q was multiplied by 76, which was found in preliminary studies to fit the experimental crystallization flow rates. Experimentally, this could mean that the synthesis is performed by using 76 parallel tubes.

The ASA concentration in the quenched reaction mixture was used to calculate the c_0 inlet concentration in the crystallizer:

$$c_{in} = \frac{c_{q,ASA}}{AS+1} \tag{39}$$

(In the synthesis models, molar concentrations are calculated, whereas in the crystallization step these were converted into kg m^{-3}.) For the integrated simulations, the crystallization model was amended to also take into account the possible effect of the impurities (considering the sum of $c_{q,A}$ and $c_{q,B}$) on the crystallization kinetics. It is important to note, that we have no experimental data about the impurities influencing the crystallization, that is, this aspect of the study is purely for simulation purposes. However, the available literature suggests, that for example, Impurity B (acetylsalicylic anhydride) may have an impact on the crystallization kinetics of ASA [37,38].

The crystal growth in the presence of the impurity was described using the model of Kubota and Mullin [39,40], where the impurities are assumed to be absorbed in kink sites with a pinning mechanism and with increasing surface coverage, this results in the linear decrease in the step velocity. By using the Langmuir adsorption isotherm, the step velocity can be related to the impurity concentration of the solution and with the assumption that the growth rate is proportional to the step velocity, the expression of the growth rate (Eq. (29)) is modified to

$$G(\sigma, T, c_i) = G_0(\sigma, T) \cdot \left[1 - \frac{\alpha K_L c_i}{1 + K_L c_i}\right] \tag{40}$$

where K_L [kg m^{-3}] denote the Langmuir constant and α [-] is the effectiveness factor, that indicates how efficiently the impurity inhibits the crystal growth. When $\alpha > 1$, the growth rate decreases fast to reach 0 even at small $K_L c_i$ values, at $\alpha = 1$ the growth rate approaches zero asymptotically, while for $\alpha < 1$ it approaches a non-zero value. Although different impurity species can exhibit different effectiveness, for simplicity, in this study Impurity A and B were treated together. Consequently, the impurity concentration c_i was expressed as:

$$c_i = c_{q,A} + c_{q,B} \tag{41}$$

As there were no experimental data available to estimate K_L and α, different values were tested in sensitivity analysis to investigate their effect on the integrated model.

The *in vitro* dissolution prediction model was connected downstream the integrated production of ASA with the assumption that appropriate filtration and drying occur between the crystallization and dissolution testing. These steps were studied by the authors of this paper [28,30]. It is also assumed that the moisture content of the ASA powder can be neglected after filtration and drying, that is the mass flow rate of the ASA powder ($\dot{m}$) can be directly calculated from the crystallization model:

$$\dot{m} = F_c \cdot c_s \tag{42}$$

where c_s denotes the solid concentration in the crystallization slurry. The dissolution model constantly performed the surrogate dissolution test with an m_c sample mass every time a predefined m_{prod} product mass is collected from the continuous line. The CSD of the sample is the average of the CSDs calculated by the crystallization during the

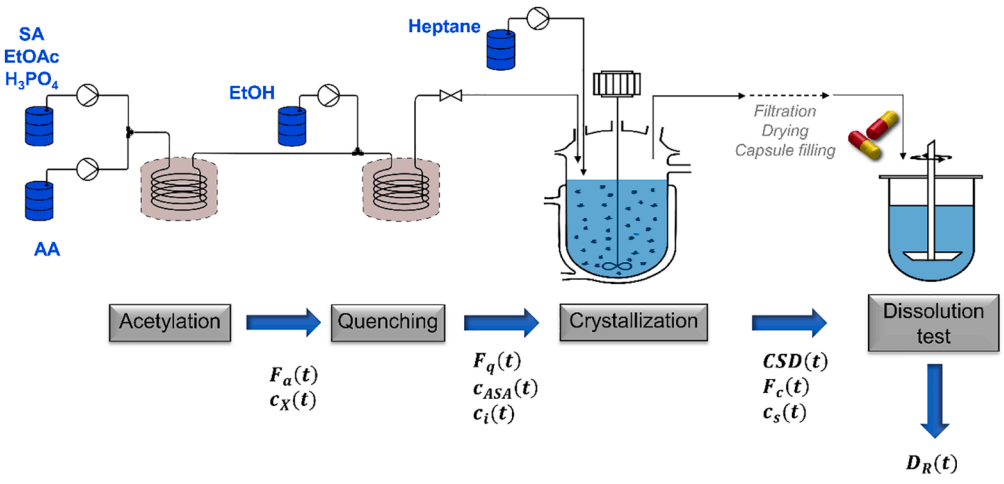

Fig 1. Dynamic flowsheet model of continuous ASA production.

timeframe of the intermittent product collection. In this work, the value of m_{prod} was set to 1000 mg, which means the dissolution testing after 10 dosage units, however, it can be set to any arbitrary value *e.g.,* to fit the sampling frequency requirements of the regulatory guidelines.

2.3. Simulation case studies on the developed flowsheet model

2.3.1. Optimization studies

Optimization studies of the standalone synthesis, crystallization, as well of the integrated process were performed and compared. The optimization of the synthesis steps was conducted by calling the *fmincon* optimization function of Matlab® with the default interior-point algorithm. The integrated flowsheet model was optimized in the Simulink Design Optimization Toolbox, where the sequential quadratic programming algorithm was used.

For the synthesis, five process parameters were chosen to be optimized: the temperature of the acetylation (T_a) and quenching reactor (T_q), the amount of AA (AA_{eq}) and EtOH ($EtOH_{eq}$) expressed as the mole equivalent of the initial SA and the residence time in the acetylation reactor (τ_a), which, together with AA_{eq} and $EtOH_{eq}$, determines the residence time in the quenching reactor, too. Additionally, the constraint of $EtOH_{eq} \geq AA_{eq}$ was used to ensure that the quenching reactor can result in the total decomposition of AA. The synthesis optimization aimed to obtain the highest conversion (X) at the end of the operation (as the objective function, -X was minimized):

$$X[\%] = \frac{c_{ASA} + c_A + c_B}{c^0_{a,SA}} \cdot 100 \tag{43}$$

Additionally, the purity (P) of the obtained reaction mixture was also calculated as Eq. (44).

$$P[\%] = \frac{c_{ASA}}{c_{ASA} + c_A + c_B + c_{SA}} \cdot 100 \tag{44}$$

When the crystallization and the integrated continuous manufacturing line was studied, the crystallization operation parameters of T_c and AS were also included as decision variables. In this case, the overall productivity [g h^{-1}], the mean particle size (D[1,0], *i.e.,* the arithmetic number mean of the CSD), and the dissolution properties (T85, *i.e.,* the dissolution time necessary for the dissolution of the 85% of the API) were the objectives with equal weight. As τ_a, AA_{eq}, $EtOH_{eq}$ and AS are optimized, and the crystallizer is assumed to be operated in a constant volume, the residence times in the quenching reactor (τ_q) and the in the crystallizer (τ_c) are also defined by these parameters, that is remained no freedom to independently vary τ_c during the optimization. Nevertheless, one could vary the slurry level in the crystallizer to manipulate the mean residence time, but due to technical limitations (including the stirring effectiveness), this range is limited, therefore, in this work, it was decided to fix the crystallizer volume. Consequently, for comparability with the integrated process, even in the stepwise optimization case, τ_c was not handled as a decision variable.

2.3.2. Sensitivity analysis

Two separate sensitivity analysis studies were conducted to analyze the effect of uncertainty of the operational parameters (the parameters used in the optimization studies) as well as the kinetic parameters on the CQAs. For the latter, 11 parameters were used: the k_1, k_3, k_4, k_5, k_7 and k_{7r} reaction rate constants, k_b, k_g, K_L and α of the crystallization model and k_d for the dissolution process.

For screening and ranking the importance of the parameters, the Morris method, also called the elementary effect test [8,41], was used, which is a multiple-start, global perturbation method. Perturbation methods vary (perturb) the input factors ($\bar{x}_1,\ldots\bar{x}_i,\ldots,\bar{x}_N$) one-at-a-time (OAT) from the nominal value and quantify their effect on the g scalar output by calculating the partial derivatives. As the analytical form of the input–output relationship is rarely known, this is approximated by the finite differences:

$$EE^j = \frac{g\left(\bar{x}_1, \cdots, \bar{x}_i + \Delta_i, \cdots, \bar{x}_N\right) - g\left(\bar{x}_1, \cdots, \bar{x}_i, \cdots, \bar{x}_N\right)}{\Delta_i} c_i \tag{45}$$

where $(\bar{x}_1, \cdots, \bar{x}_i + \Delta_i, \cdots, \bar{x}_N)$ denote the i^{th} perturbation and c_i is a scaling factor to facilitate the comparison of the input factors having different units. In the Morris method, this finite difference is called the elementary effect (EE). To make the method global, *i.e.,* to consider the variation within the entire variability space of the input parameters, r EEs are computed within the input space, and the mean (μ_M) and standard deviation (σ^2_M) of the EEs' distribution function are used as sensitivity indices:

$$\mu_M = \frac{1}{r} \sum_{j=1}^{r} EE^j \tag{46}$$

$$\sigma^2_M = \frac{1}{r-1} \sum_{j=1}^{r} \left(EE^j - \mu_M\right)^2 \tag{47}$$

To assess the sensitivity of the output to the inputs, μ_M and σ^2_M are analyzed in parallel. A high μ_M value indicates the high influence of the given input factor and a high σ^2_M means that the sensitivity changes across the variability space, which can be either caused by a non-linear effect or because of the interaction with the other factors. In this work, the productivity, D[1,0], T85, the impurity and ASA concentration after quenching and the solid concentration of crystallization were used as g outputs.

Several strategies exist for the selection of the $\bar{x}_i$ sampling points and Δ_i variations, which are discussed in detail elsewhere [8]. In this work, the radial design OAT sampling strategy [42] was used where the Δ_i variations were taken from the same $\bar{x}_i$ points, selected based on a Latin Hypercube.

As the calculation of one EE (Eq. (45)) requires $(N + 1)$ model evaluations, a total of $r(N+1)$ simulations are required for performing the Morris analysis, which is computationally cheap compared to other, *e.g.,* variance-based global sensitivity analyses. As a rule of thumb, the number of r is usually advised to be around 10-100N to reach convergence and obtain the indices with satisfactory confidence intervals for ranking. This was reached using 125 EEs in the analysis of the operational parameters (meaning a total of 1000 model evaluations), whereas the sensitivity of the kinetic parameters was studied using 40 EEs (480 total simulations). All the calculations related to the sensitivity analysis (sampling, calculation of Morris indices, confidence intervals, and the analysis of convergence) were performed using the SAFE toolbox [43,44].

3. Results and discussion

3.1. Parameter estimation results

The parameter estimations were performed using different combinations of the possible kinetics (*e.g.,* accounting or neglecting the reversibility of a reaction) and reaction schemes (*e.g.,* considering the different possible reactions (Eq. 1.a-1.d) during acetylation) to find the best fit to the experimental results. In the case of the acetylation process, the models also used different experimental data.

Table 6 summarizes the considered kinetic models for acetylation and the obtained errors for the batch ($Error_b$) and continuous ($Error_c$) validation samples. These errors were calculated the same way as $O(D)_{batch}$ and $O(D)_{cont}$ during the parameter estimation (see Eq. (20, 21)), with the exception that for the continuous validation data, $w = 0$ was applied in Eq. (21), that is the nMSE values of the ASA, SA and impurity concentration predictions were summarized. Comparing *Model 1* and *2*, it is apparent that both models utilize only the batch calibration data, however $Error_b$ and $Error_c$ were significantly lower than in *Model 2*. This was caused by the difference in accounting the formation of Impurity A: while *Model 1* assumed that the formed ASA takes part in subsequent acetylation (Eq. (1.b)), it was found that the simulations fit better the experimental data when Impurity A is assumed to be produced by the double acetylation of SA with the excess AA (Eq. (1.d)). Therefore, in further investigations only the latter route was accounted.

Utilizing the batch or continuous calibration data did not result in such considerable changes in the validation error values and the most substantial difference occurred in the confidence intervals. Fig. 2 illustrates the fit of prediction with *Model 2–4* to the experiment of A_{batch} *Val 2*. The same conclusions could be drawn from the other two validation experiments. Although Fig. 2 suggests a relatively simple polynomial form as the dynamics, it needs to be accounted that for the model fitting, 10 parameters (see Table 6) needed to be simultaneously estimated, using the ordinary differential equation systems detailed in Section 2.2.1 and Appendix A.1, while relatively small experimental dataset was available for fitting. This is the reason for the wider confidence intervals (also seen in Figs. 3 and 4), and given these limitations, the model fit could be deemed to be satisfactory to estimate the dynamics of the process. It also needs to be noted, that the concentration of Impurity B is one order of magnitude smaller than that of the other parameters, therefore the seemingly big difference between the measured and predicted concentrations in Fig. 2. Although at *Model 3*, the parameter estimation was performed using only steady-state concentration data, it is apparent, that it could also describe the dynamics of the batch process with comparable accuracy as *Model 2*. However, the wider confidence intervals indicate a higher uncertainty of the parameters, which could be explained by the smaller continuous dataset used for the estimations *i.e.,* only steady-state concentrations were available. This also appeared in continuous validation results (Fig. 3). *Model 4*, where continuous and batch data were used combined, provided similar results to *Model 2* for

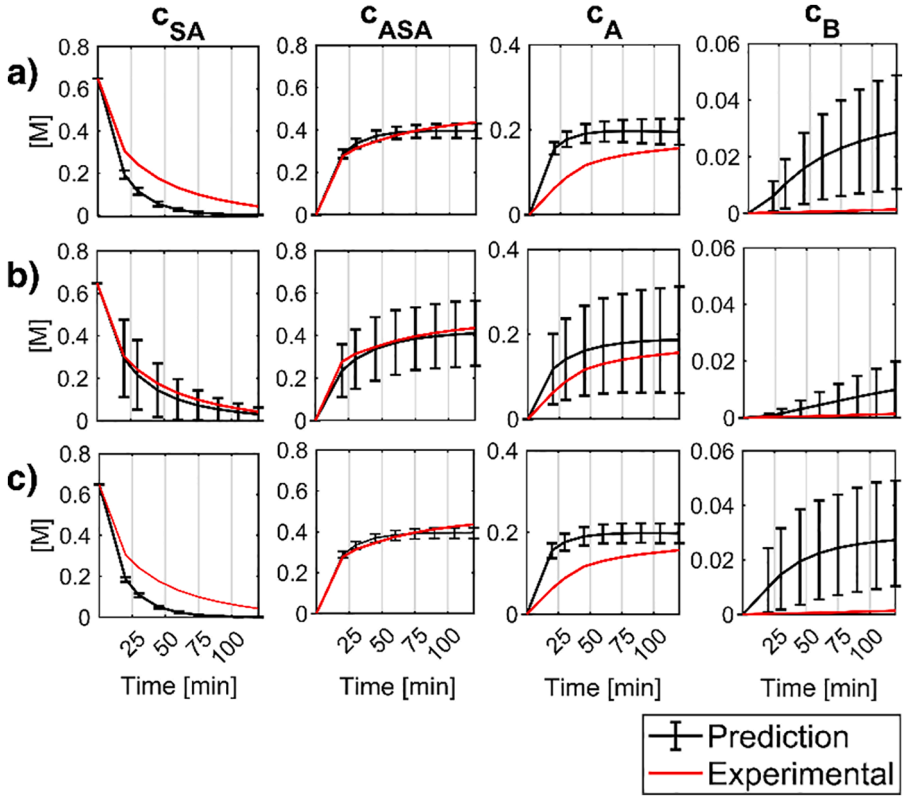

Fig 2. Predicted and measured concentration for A_{batch} Val 2 setting with a) Model 2, b) Model 3, c) Model 4.

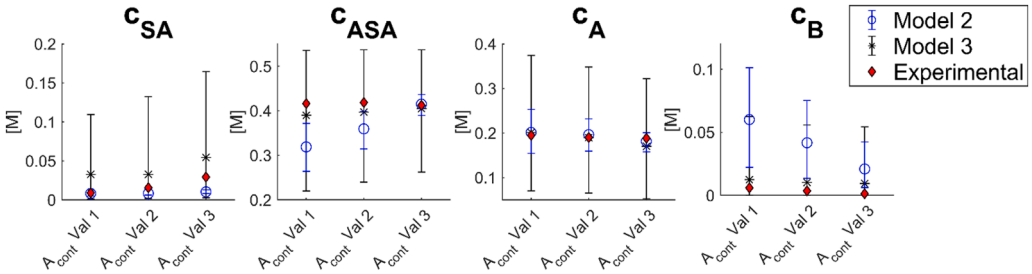

Fig 3. Predicted and measured concentrations for the continuous validation acetylation settings with Models 2 and 3.

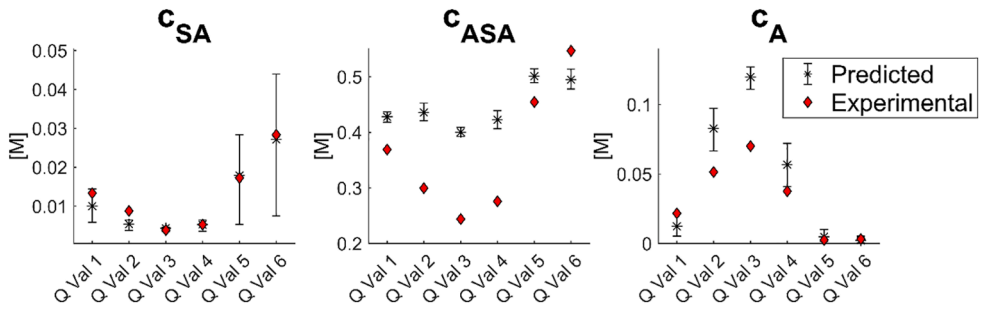

Fig 4. Predicted and measured concentration for the quenching validation experiments.

both the batch and continuous validation results, with slightly different confidence intervals, therefore *Model 4* is not depicted in Fig. 3. The SA concentrations of the continuous validation experiments were overestimated with *Model 3*, while higher inaccuracies in the ASA content were observed with *Model 2*. However, the trends between the different experimental settings were followed better with *Model 3*, therefore, the kinetic parameters of *Model 3* were used in the integrated flowsheet model. In Fig. 3, the effect of the decreasing temperature and the simultaneous increase of the residence time (see Table 1) can be followed: from A_{cont} *Val 1* to *3* the ASA and SA concentrations were increased slightly, while the amount of the impurities decreased. The analysis of the effect of the operating conditions on the concentrations is detailed in Section 3.3.

Several combinations of the kinetic parameters and reaction schemes were also tested for the quenching step of the synthesis, however, there were no substantial differences observed in the quality of the fit, therefore in Table 7, only the final parameters are summarized. The validation error was calculated the same way as explained in the case of acetylation. It is notable that A_6 and $E_{a,6}$ are fixed to 0, which is explained by the fact that there was no available experimental data about the concentration of the EtOAc, HA and EtOH after quenching. However, in preliminary parameter estimation calculations the value of $k_6$did not influence the concentration of the other components. Therefore, with the assumption that the total decomposition of AA completes fast in the quenching reactor, this reaction was neglected. Furthermore, having only the limited dataset of continuous steady-state measurements, the activation energies were fixed to values found adequate during the preliminary studies to decrease the uncertainty of the parameter estimation. Fig. 4 shows that the quenching model could predict the concentration variations caused by the different operations of the quenching reactor. The temperature and the residence time in the quenching reactor and the EtOH amount were varied simultaneously in the validation experiments (see Table 2). It is visible that in the case of *Q Val 5–6*, the SA concentration could be determined with higher uncertainty, which is associated with the longer residence times. However, the variability of the calculated ASA concentration was lower than that of the experimental values, which indicates that effects associated with the changes in ASA concentration might be underestimated when the model is utilized in the flowsheet simulation. As the trends depicted in Fig. 4 show the simultaneous variation of the three operational parameters, the analysis of these effects is complicated, but it is further addressed in the sensitivity studies (Section 3.3).

Although some of the kinetic parameters for the acetylation and quenching step could be estimated only with wide confidence intervals, which suggest that the parameters are correlated and the resulting uncertainty space is relatively large, yet the nominal values of the parameters were found to provide a satisfactorily good agreement with the experimental results. This shows that by using the nominal parameters, the models can be used for further analysis of the operational parameters' effect. Also, based on these parameter estimation results, one could carry out a robust optimization, which directly involves the parameter uncertainties. To further address the question of the effect of the parameter uncertainty, the kinetic parameters were also studied by sensitivity analysis (see Section 3.3), to revealed which parameters are critical. In future work, the confidence interval of these parameters could be reduced by utilizing more experimental data for the parameter estimation.

The parameter estimation of the dissolution model resulted in the substantial simplification of the dissolution rate expression (Eq. (33)) because it was found that the p_1 and p_2 take extremely uncertain values as well their value did not influence the accuracy of the prediction. This resulted in the simplification of the size-dependent term into size-independent dissolution expression. Although it is well known that the smaller particles dissolve faster, these effects are significant at nanoscale, but the size dependency of the solubility vanishes over a few micrometers. In this study, the initial particles exposed to dissolution were generally well over this size range and the majority of the solids are already dissolved when the particles shrink to this size. Therefore, the simulated concentration curve remains valid in the solute concentration variation domain of interest and this explains the adequacy of the size-independent dissolution rate. Regarding d and k_d, since a low amount of solid was dissolved relative to the solvent volume and the experiments were performed under sink conditions, meaning that the change in the supersaturation is not relevant, it was impossible to decouple d from k_d and therefore d was fixed to 1. The final kinetic model (see Table 7) including only the dissolution rate coefficient was suitable for the surrogate modeling of the dissolution curve of the validation samples (Fig. 5).

As for the dissolution of the ASA filled into capsules, the experimental capsule dissolution curves (green lines in Fig. 5) exhibit a slower release compared to the powder measurements, but no lag time was observed due to the dissolution of the capsule shell, as it started to dissolve within the first two minutes of the test. Therefore, the assumption of the constant retarding effect was found to be adequate for this case, and the multiplication of the dissolution rate ($D(\sigma_d, L)$) by the constant retarding factor of 0.5 was found to provide a reasonably good fit as seen in Fig. 5. This approach is admittedly a significant simplification, which is not suitable for several capsule formulations *e.g.,* due to the possible API-excipient interactions or a potential lag time caused by the slow dissolution of the capsule shell, in which cases further model development would be necessary. However, such a simplified method could contribute to a better understanding of the effect of the crystal size distribution as CMA and the corresponding optimization and risk analysis of the manufacturing process of the API during the early stage of the drug development.

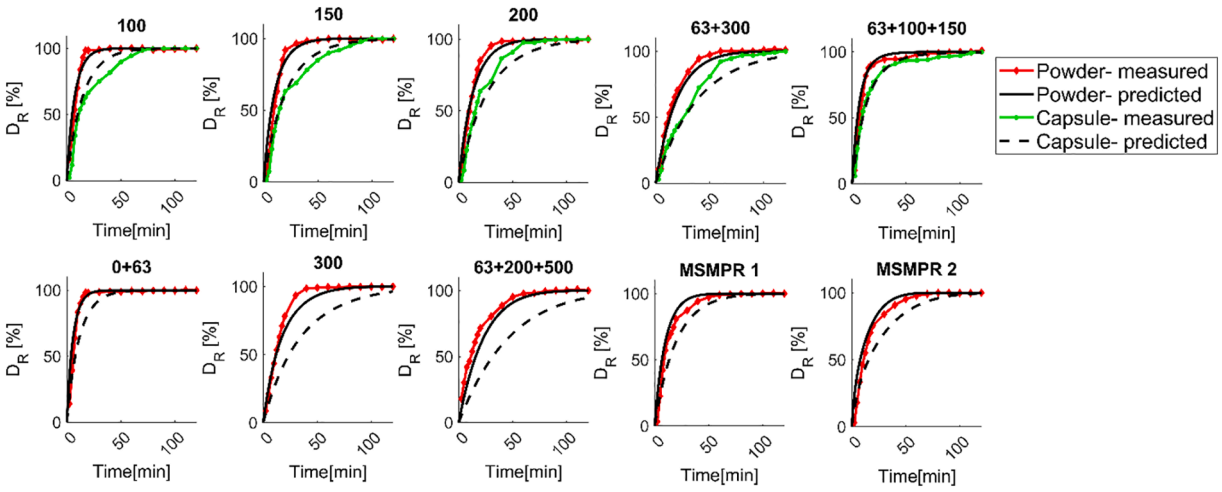

Fig 5. Predicted and measured validation experiments for the validation dissolution samples.

3.2. Optimization of the integrated continuous line

To investigate how the integrated flowsheet simulation can contribute to better understanding and operation of the continuous manufacturing line, several optimization problems were defined and solved. First, the standalone synthesis was considered, followed by the examination of the integrated synthesis and crystallization processes. The goal of this comparison is to compare the achievable product quality attributes if all operations are optimized individually subject to local objectives *vs.* the plant-wide optimization of the integrated process using the developed flowsheet model. In the former approach the operating parameters of the synthesis were optimized in three stages: in the first stage the optimal value of AA_{eq} was determined using batch acetylation, along with an optimal batch T_a. In the next stage, the flow acetylation process parameters (τ_a and T_a for the continuous reactor) were optimized while AA_{eq} was fixed for the value found optimal in the batch acetylation. In the last step, the quenching parameters (T_q and $EtOH_{eq}$) were optimized with the fixed acetylation process. Compared to this, in the second approach, all parameters could be simultaneously optimized. The optimization results are summarized in Table 8.

While the 3-stage procedure is identical to the experimental optimization procedure [28] and is a common practice to reduce the necessary number of experiments, the simulation results clearly showed the advantages of considering the reactor cascade in the optimizations. Table 8 shows that the integrated process optimization resulted in 10% higher conversion compared to the step-by-step procedure. Moreover, this was achieved along with the significant increase in the purity of the reaction mixture, too, which can further simplify the purification (*e.g.,* crystallization) steps. The most substantial difference in the operation parameters of the two approaches could be found in the applied AA and EtOH excess. It is apparent, that in the batch acetylation stage of the step-by-step approach, the optimal value of AA_{eq} was fixed to the upper boundary along with a relatively low temperature, as the excess AA promotes the conversion of SA in the acetylation step, which also resulted in high necessary $EtOH_{eq}$ in the quenching step. However, as the integration optimization indicated, it was beneficial from the point of the global conversion to process an acetylated reaction mixture with lower conversion (87.4% as opposed to 93.5% of the step-by-step method) than aiming for maximal conversion at each stage. The lower amount of AA and EtOH could be compensated with higher temperatures and longer residence time. At this stage of the work, the integrated results have not been directly experimentally validated, yet. However, as the models of all the unit operation are individually validated and the acetylation and the quenching model steps were directly integrated without further assumptions (*i.e.,* all the obtained component concentrations after acetylation were used in the quenching model), it can be expected that the integrated calculation does not influence the validity of the results. Also, the comparison of the stepwise optimization simulations with the experiments (see [28]) showed good agreement, *e.g.,* the experimental batch acetylation optimization suggested high AA_{eq} value, but it also promoted the formation of the impurities, whereas the increase of the temperature and residence time increased the purity in the flow acetylation.

The integrated continuous synthesis- crystallization process was optimized to provide the highest productivity [g h^{-1}]. This was also done in different ways: first, the synthesis process was fixed to the "Stage 3" and "Integrated synthesis" conditions from Table 8 and the crystallization process parameters (T_c and *AS*) were optimized, then the entire reaction-crystallization cascade was optimized in an integrated way. In the first case, the synthesis settings of both the previous step-by-step (*Fixed synthesis 1* in Table 9) and integrated approach (*Fixed synthesis 2* in Table 9) were tested to examine whether optimized crystallization

Table 8
Optimization results of the synthesis step with the step-by-step and integrated approach. The allowed parameter ranges are given in parenthesis next to the parameter names.

	Stage 1- Batch acetylation	Stage 2-Flow acetylation	Stage 3- Flow quenching	Integrated synthesis
AA_{eq} [-] (1–10)	9.99	***9.99 (fix)***	***9.99 (fix)***	1.22
T_a ***(batch)*** [°C] (0–100)	28.01	–	–	–
T_a ***(cont.)*** [°C] (0–150)	–	80.22	***80.22 (fix)***	150.00
τ_a [min] (60–300)	–	82.65	***82.65 (fix)***	100.14
T_q [°C] (0–150)	–	–	40.06	78.81
$EtOH_{eq}$ [-] (1–15)	–	–	10.00	1.22
Conversion after acetylation [%]	99.8	93.5	93.5	87.4
Purity after acetylation [%]	64.9	52.6	52.6	87.1
Final conversion [%]	–	–	**72.5**	**82.8**
Final purity [%]	–	–	**60.4**	**87.6**

Table 9
Optimization results of the integrated process. The allowed parameter ranges are given in parenthesis next to the parameter names.

	Fixed synthesis 1	Fixed synthesis 2	Integrated synthesis + crystallization	Multi-objective optimization
AA_{eq} [-] (1–10)	***9.99 (fix)***	***1.22 (fix)***	1.00	1.00
T_a ***(cont.)*** [°C] (0–150)	***80.22 (fix)***	***150.00 (fix)***	150.00	150.00
τ_a [min] (60–300)	***82.65 (fix)***	***100.14 (fix)***	60.00	60.00
T_q [°C] (0–150)	***40.06 (fix)***	***78.81 (fix)***	76.69	57.57
$EtOH_{eq}$ [-] (1–15)	***10.00 (fix)***	***1.22 (fix)***	1.00	5.21
T_c [°C] (0–50)	40.66	42.30	39.52	21.55
AS [-] (1–8)	8	7.70	8	8
Conversion after synthesis [%]	72.5	82.8	77.0	63.5
Purity after synthesis [%]	60.4	87.6	80.2	79.4
Overall productivity [gh^{-1}]	**12.6**	**24.6**	**40.6**	**30.5**
D[1,0] [µm]	86.4	91.9	84.8	**41.6**
T85 [min]	27.9	29.7	27.4	**14.0**

could compensate for the different conversion in the reaction mixtures. As seen in Table 9, to obtain high productivity, high antisolvent-solvent volume ratios are suggested, while the relatively high crystallization temperatures could be associated with the high activation energy of the crystal growth [30]. It is noticeable, that the optimized crystallization settings for both *Fixed synthesis 1* and *2* resulted in similar values, yet the higher conversion rate in the synthesis provided a doubled productivity of the final ASA product. This suggests that even the optimization of the multi-step synthesis as a unit can result in a vast improvement in the overall performance of continuous manufacturing. Nevertheless, when the synthesis-crystallization process was studied in an integrated way, the productivity could be further increased to 40.6 g h^{-1}, which was mainly associated with the decrease of the residence time. The calculated synthesis conversion value was between the settings of the two previously studied syntheses, which further emphasizes that the standalone optimization of the synthesis, without the crystallization step, is not sufficient to reach maximum productivity at the end of the continuous line.

In summary, the integrated plant-wide optimization resulted in a 3.2-fold overall productivity improvement compared to the optimization of individual units, which clearly demonstrates the benefit of the development of flowsheet simulations. Furthermore, these results were reached with lower excess of AA and EtOH, that is not only the productivity is increased, but the material costs and environmental footprints are also reduced. The conclusions drawn from these optimizations could contribute to the experimental integration of the unit operation with fewer but more targeted experiments. Therefore, future studies will aim the experimental realization of the above results, which could also validate the integrated flowsheet model.

As most of the pharmaceutical manufacturing processes are not solely aims to maximize the productivity, but also to achieve pre-defined properties of the final product, a multi-objective optimization was also performed using the integrated flowsheet model. In this case, besides the maximization of the productivity, the mean particle (D[1,0]) was also aimed to be maximized, as this significantly influences the downstream processability, such as the filtration [30] or blending. However, as the particle size also affects the dissolution properties, the additional constrain of the dissolution of the ASA capsules was also added. This was defined such as the T85, *i.e.,* the dissolution time necessary for the dissolution of the 85% of the API, must be equal to or<15 min in 0.1 N HCl. This criterium ensures for high solubility, high permeability (BCS I) drugs, like ASA, that the bioavailability is not limited by the dissolution, therefore it can be regarded as an immediate-release formulation [45]. As the results in Table 9 shows, this was achieved by the reduction of T_c and T_q and the applied EtOH amount was also increased. While the additional objective and constraint reduced the productivity to 30.5 g h^{-1}, this could be still regarded as relatively good productivity and represents a good trade-off for product quality. However, to fulfill the dissolution criteria, the particle size had to be significantly reduced compared to the previous results. The 41.6 µm D[1,0] value can be associated with good filterability [30], but flowability problems might occur which may need to be addressed.

3.3. Sensitivity analysis

Sensitivity analyses were conducted at the operation point of the process at the settings obtained by the multi-objective optimization (last column in Table 9). The identification of the effects and risks associated with the involuntary changes in the process parameters and the uncertainty in the kinetic parameters of the simulation was the objective. This way, the flowsheet modeling can help to understand the development and operation of the integrated continuous manufacturing lines better and it also contributes to the determination of PAT and control strategies.

To study the sensitivity of the operational parameters, first, the input variability space had to be defined. This can be performed based on experimentally observed uncertainty and process characteristic. It was assumed that the uncertainty of the operating parameters occurs due to the random disturbances, which are handled as normally distributed random variables. The standard deviations (STDs) of the distributions were first defined as the 20% of the mean for each parameter, then in a second run it was refined such as the STDs of AA_{eq}, *AS*, $EtOH_{eq}$ and τ_a were 10% of the mean values, but 5, 5 and 20% forT_a, T_q and T_c, respectively. This was determined based on the experimental observations that T_a and T_q can be kept at the required value very well, but T_c showed high uncertainty during the processes. The two runs did not show significant differences, therefore only the results of the second are presented here in detail.

The simulated parameter space is illustrated in Fig. 6 with the color scale indicating the steady-state productivity values. The dynamic responses of the simulations can be seen in Fig. 7, which can help analyze the error propagation through the system. It is noticeable that the uncertainty of the input space significantly affects the output variability considering either the productivity, the crystallization slurry properties, or the reaction mixture concentrations. With 95% confidence, the productivity was found to be varying between 16.0 and 39.3 g h^{-1}, however, some extreme parameter combinations exhibited strong detrimental effect resulting in productivity below 10 g h^{-1}. The D[1,0] and T85 values were found to be varying between 26.6 and 64.4 and 10.4–20.0 min, respectively, the latter meaning, that the risk of failing the immediate-release specification is very high. The cumulative distribution functions (CDFs) of the parameters belonging to the immediate-release and the out-of-specification T85 values (Fig. 6) showed no difference for any of the parameters but the T_c, where two distinct CFDs were observed: the one belonging to the immediate-release capsules ranging from 0 to 23 °C, while the out-of-specification setting starting at 23 °C. This highlights that keeping T_c under 23 °C is vital for obtaining the required quality of the capsules, which must be addressed

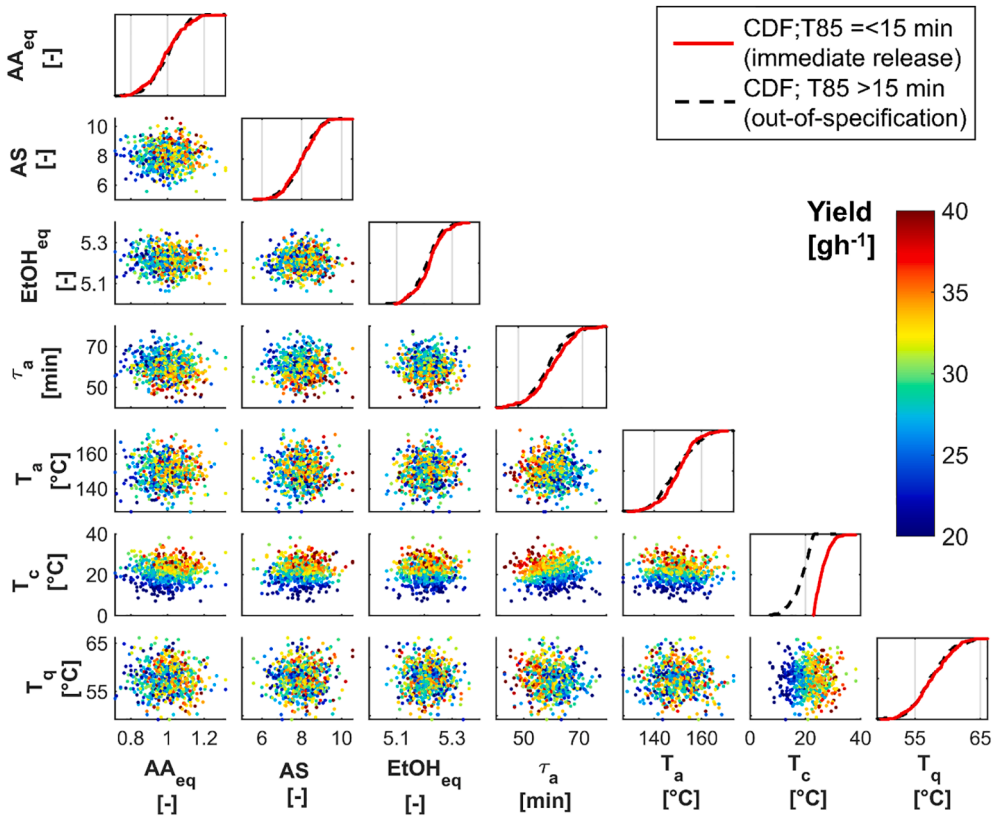

Fig 6. The simulated input parameter space (1000 model evaluations) and the cumulative distribution functions of the simulations belonging to the immediate-release and out-of-specification dissolutions. The color of the dots represents the productivity obtained with the given parameters. The readers are referred to the on-line version of this paper for the colored figure.

when developing the control strategy.

As for disturbance propagation, it is visible from Fig. 7, that the productivity and the mean particle size change immediately (within a few minutes) after the change of the parameter from the steady state of the nominal operational parameter. However, 8 min lag-time was observed at the change of the dissolution property, followed by a slower, gradual transition lasting about 30 min. The variation in the concentrations of the final reaction mixture was also studied, which also revealed an approximately 5 min lag-time with a long transition time, which could be associated with long residence time in the flow reactors.

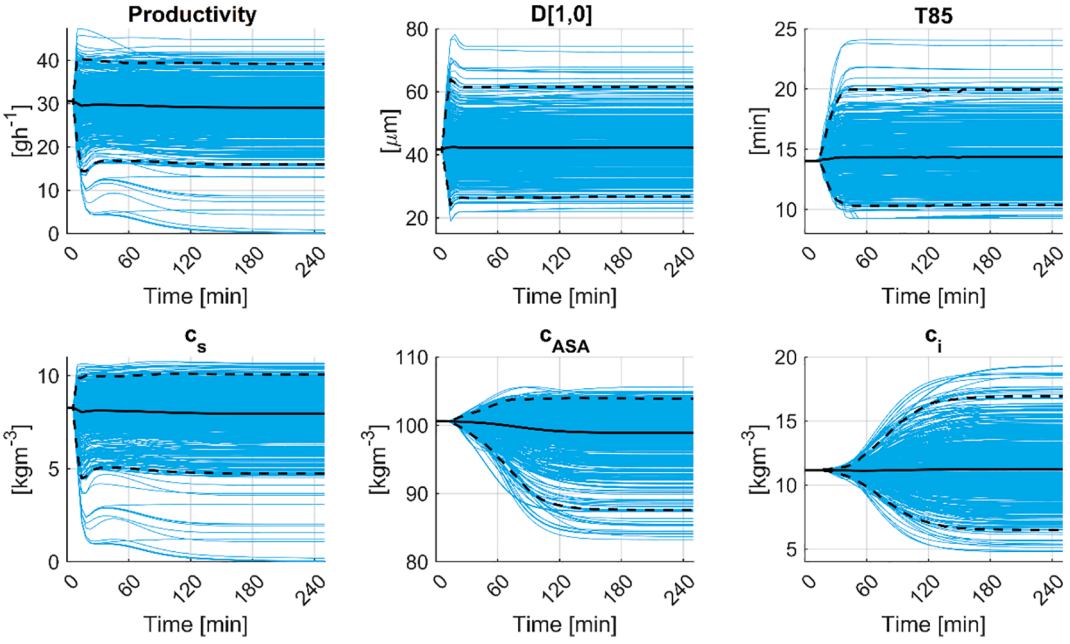

Fig 7. Output uncertainty along the simulation time. The solid and dashed black lines represent the mean and the 95% confidence interval of the 1000 model evaluations, respectively.

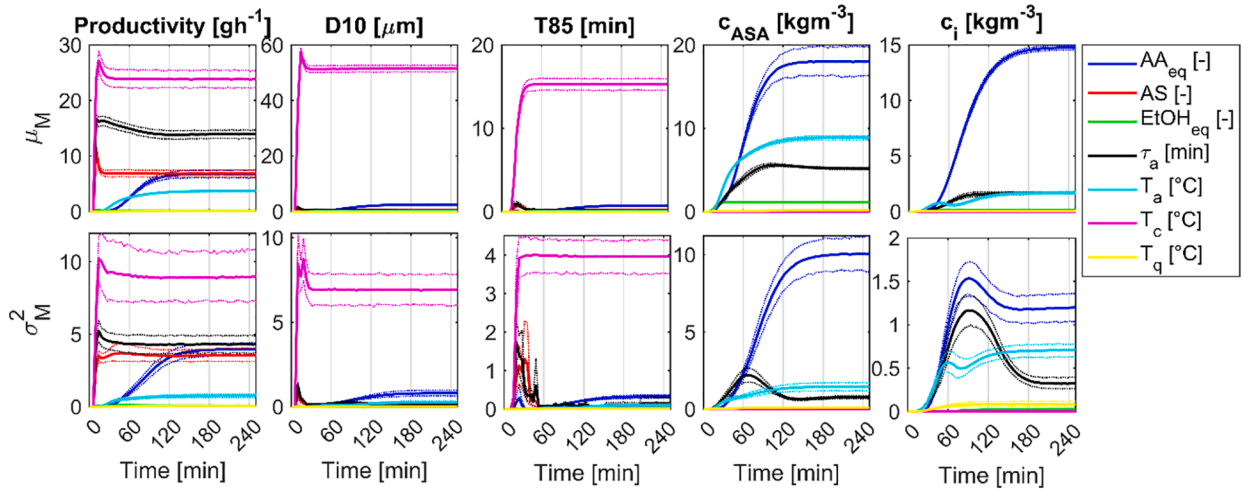

Fig 8. Time-varying Morris sensitivity indices. The dotted lines represent the 95% confidence interval of the indices.

The Morris indices calculated for each simulation time point helped understand these observations better (Fig. 8). Starting with the mean particle size, the greatest μ_M and σ_M^2 values were obtained for T_c, whereas the indices of other parameters were insignificant. As the dissolution properties of the final capsules are calculated based on the CSD, it was expected, that for the T85, T_c also emerged as the most influential parameter. However, in the first hour of the simulation, the relatively high σ_M^2 of τ_a and *AS* indicate their non-linear effect or interaction with other parameters, which can be the explanation of the slower transition to the new T85 value. Moving on to the concentrations of ASA and impurity in the reaction mixture, the three operating parameters of the acetylation step were identified as significant, among which AA_{eq} resulted in the highest μ_M and σ_M^2. The dynamic representation also allows noticing that during the transitional state, the non-linear effect or interactions associated with AA_{eq} and τ_a changes non-monotonically, which might be caused by the multiple, concurrent reactions influencing the concentrations. The most complex outcome of the sensitivity analysis was discovered for the overall productivity. While T_c appeared again as the most influential parameter, the *AS* and τ_a also exerted an immediate effect. It needs to be noted that the high impact of T_c was not only resulted due to its defined higher uncertainty, but the same importance was observed when the STDs of all parameters were defined equal. AA_{eq} showed comparable results as *AS*, however, its effect evolves gradually in 120 min. These results further reinforce the observations of the optimization study, too, *i.e.,* it is critical to control the whole integrated process as a system, to ensure consistent and satisfactory productivity. Another important conclusion of the sensitivity analysis, that the parameters of the quenching unit ($EtOH_{eq}, T_q$) were not found significant for any of the analyzed objectives, which suggests that this might be the most robust unit and its control is less vital than that of the acetylation and crystallization.

With the sensitivity analysis of the kinetic parameters, the question of the uncertainty of the developed model was addressed. Although the confidence intervals of the kinetic parameters indicate the parameter uncertainty, it was too wide to be further used in the sensitivity analysis, as it resulted in several computationally infeasible parameter combinations. Therefore, the uncertainty of all parameters was defined as normal distributions, the mean being the estimated parameter (see Tables 4, 6 and 7) and using the 5% of the mean value as the STD. The results of the Morris screening are illustrated in Fig. 9 for the steady state of the productivity, mean particle size and dissolution property. The productivity was found to be influenced by α, *i.e.,* the effectiveness factor of the impurities, as well as by k_1 and k_4, that is the reactions when SA is converted into ASA and Impurity A. The D[1,0] was found to be mainly affected by α, k_d and the crystallization kinetics (k_b, k_g) had a significant effect on the dissolution of the ASA capsules.

The results of the sensitivity analysis of the operating parameters and the kinetics parameters support each other as the importance of the crystallization is clearly revealed in both cases as well as the productivity is found to be influenced by both the acetylation and crystallization steps, while the uncertainty in the quenching kinetics was found to be less important. The most noticeable is the great impact of α, which is a clear indication that whenever crystal growth rate inhibition by a reaction byproduct appears, this needs to be treated with extra care. Interestingly, although the Kubota model is governed by both the α and the Langmuir constant (K_L), the value of K_L was found to be insignificant in the Morris analysis. Therefore, to improve the reliability of the flowsheet model, further studies need to focus mainly on the estimation of α.

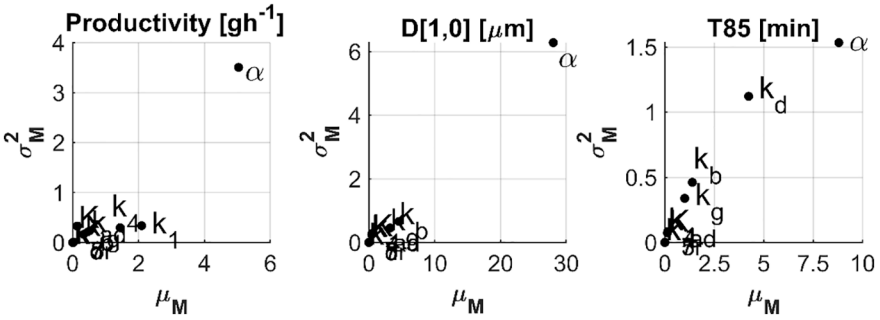

Fig 9. Morris sensitivity indices of the kinetic parameters in the steady state of the simulations.

4. Conclusions

In this work, the dynamic flowsheet model was developed for the integrated, continuous manufacturing of ASA based on the experimental data of continuous unit operations to facilitate the integration. Together with our previous work on the modeling of continuous filtration [30], the dynamic model of the fully integrated, continuous upstream manufacturing was achieved. The optimization of the integrated process resulted in a significant overall productivity increase compared to the step-by-step optimization of the unit operations, and at the same time, the excess of the reactants could be decreased, which highlights the impact of the flowsheet modeling on the economic and environmental-friendly operation of the manufacturing.

Furthermore, the surrogate model of the *in vitro* dissolution test of ASA capsules was integrated into the flowsheet model the first time, which enabled the risk analysis of the failure of the dissolution specifications of an immediate-release formulation. The presented dissolution model is directly applicable for capsule formulations where the excipients, *e.g.,* fillers or diluents do not influence the dissolution rate and hence the only critical factor is the CSD, but it might be also useful in the case of more complex formulations to analyze the effect of the CMAs individually and optimize the manufacturing accordingly. Future work will also address the modeling of further formulations (*e.g.,* tablets) and their integration into flowsheet models when multiple critical material attributes and process parameters need to be accounted. The calculation of the time-varying sensitivity indices helped understand the most influential operational parameters and the risks of error propagation. Although the presented dissolution model was developed for a fairly simple formulation (*i.e.,* capsules, where the CSD of the API determined the dissolution property), the presented work indicates its importance, and hence it could encourage further studies to incorporate the dissolution model of the final formulations (*e.g.,* tablets), using either mechanistic or black-box modeling approaches. This work also highlighted the high impact of crystal growth inhibition on the final product properties.

Declaration of Competing Interest

The authors declare that they have no known competing financial interests or personal relationships that could have appeared to influence the work reported in this paper.

Acknowledgment

This work was performed in the frame of FIEK_16-1-2016-0007 project, with the support provided from the National Research, Development and Innovation Fund of Hungary, financed under the FIEK_16 funding scheme. This work was also supported from grants KH-129584, FK-132133, PD-121143 by National Research, Development and Innovation Office of Hungary and the ÚNKP-20-3 and ÚNKP-20-5 New National Excellence Program of the Ministry for Innovation and Technology. Hajnalka Pataki is thankful for the János Bolyai Research Scholarship of the Hungarian Academy of Sciences.

Appendix

A.1 Reaction network

The reaction rate equations were expressed as

$$r_1 = k_1 \cdot c_{SA}(t) \cdot c_{AA}(t) \tag{A1.a}$$

$$r_2 = k_2 \cdot c_{ASA}(t) \cdot c_{AA}(t) \tag{A1.b}$$

$$r_3 = k_3 \cdot c_A(t) \cdot c_{ASA}(t) \tag{A1.c}$$

$$r_{3r} = k_{3r} \cdot c_B(t) \cdot c_{HA}(t) \tag{A1.d}$$

$$r_4 = k_4 \cdot c_{SA}(t) \cdot c_{AA}^2(t) \tag{A1.e}$$

$$r_5 = k_5 \cdot c_A(t) \cdot c_{EtOH}(t) \tag{A1.f}$$

$$r_6 = k_6 \cdot c_{AA}(t) \cdot c_{EtOH}(t) \tag{A1.g}$$

$$r_7 = k_7 \cdot c_{ASA}(t) \cdot c_{EtOH}(t) \tag{A1.h}$$

$$r_{7r} = k_{7r} \cdot c_{SA}(t) \cdot c_{EtOAc}(t) \tag{A1.i}$$

where c_X denotes the concentration of the given reagent.

With these, the ODE system of the acetylation step can be written as:

$$\frac{dc_{a,SA}}{dt} = -r_1 - r_4 + \frac{c_{a,SA}^0 - c_{a,SA}}{\tau_a} \tag{A2.a}$$

$$\frac{dc_{a,AA}}{dt} = -r_1 - r_2 - 2r_4 + \frac{c_{a,AA}^0 - c_{a,AA}}{\tau_a} \tag{A2.b}$$

$$\frac{dc_{a,ASA}}{dt} = r_1 - r_2 - r_3 + r_{3r} + \frac{c_{a,ASA}^0 - c_{a,ASA}}{\tau_a} \tag{A2.c}$$

$$\frac{dc_{a,A}}{dt} = r_2 - r_3 + r_{3r} + r_4 + \frac{c_{a,A}^0 - c_{a,A}}{\tau_a} \tag{A2.d}$$

$$\frac{dc_{a,B}}{dt} = r_3 - r_{3r} + \frac{c_{a,B}^0 - c_{a,B}}{\tau_a} \tag{A2.e}$$

$$\frac{dc_{a,HA}}{dt} = r_1 + r_2 + r_3 - r_{3r} + 2r_4 + \frac{c^0_{a,HA} - c_{a,HA}}{\tau_a} \tag{A2.f}$$

The ODE system describing the quenching step:

$$\frac{dc_{q,SA}}{dt} = r_7 - r_{7r} + \frac{c^0_{q,SA} - c_{q,SA}}{\tau_q} \tag{A3.a}$$

$$\frac{dc_{q,AA}}{dt} = -r_6 + \frac{c^0_{q,AA} - c_{q,AA}}{\tau_q} \tag{A3.b}$$

$$\frac{dc_{q,ASA}}{dt} = r_5 - r_7 + r_{7r} + \frac{c^0_{q,ASA} - c_{q,ASA}}{\tau_q} \tag{A3.c}$$

$$\frac{dc_{q,A}}{dt} = -r_5 + \frac{c^0_{q,A} - c_{q,A}}{\tau_q} \tag{A3.d}$$

$$\frac{dc_{q,B}}{dt} = \frac{c^0_{q,B} - c_{q,B}}{\tau_q} \tag{A3.e}$$

$$\frac{dc_{q,HA}}{dt} = r_6 + \frac{c^0_{q,HA} - c_{q,HA}}{\tau_q} \tag{A3.f}$$

$$\frac{dc_{q,EtOAc}}{dt} = r_5 + r_6 + r_7 - r_{7r} + \frac{c^0_{q,EtOAc} - c_{q,EtOAc}}{\tau_q} \tag{A3.g}$$

$$\frac{dc_{q,EtOH}}{dt} = -r_5 - r_6 - r_7 + r_{7r} + \frac{c^0_{q,EtOH} - c_{q,EtOH}}{\tau_q} \tag{A3.h}$$

A.2 Determination of initial CSD for the dissolution model

The initial CSD ($n_0(L)$) for the dissolution PBM was calculated from the normalized measured CSDs (see Section 2.1.3) or the CSDs simulated using the continuous crystallization model.

$$n_0(L) = n_m(L)\frac{v_c}{\mu_3 k_v} \tag{A4}$$

where $n_m(L)$ is the normalized CSD of the sample to be dissolved (either the measured CSD of the samples detailed in Section 2.1.3 or the CSD obtained by the crystallization model), μ_3 is the third moment of the distribution (Eq.(A5)).

$$\mu_3 = \int_0^\infty L^3 n_m(L) dL \tag{A5}$$

v_c denotes the volume fraction of the sample in the dissolution medium at the initial moment, which was approximated as:

$$v_c = \frac{\frac{m_c}{\rho_c}}{\frac{m_c}{\rho_c} + V_d} \tag{A6}$$

where m_c, V_d and ρ_d correspond to the sample mass [kg], the volume of the dissolution medium [m^3] and the density of the dissolution medium [kg m^{-3}]. The values of these parameters were set following the experimental method (see Section 2.1.3) and summarized in Table 5.

References

[1] S.L. Lee, T.F. O'Connor, X. Yang, C.N. Cruz, S. Chatterjee, R.D. Madurawe, C.M. V. Moore, L.X. Yu, J. Woodcock, Modernizing pharmaceutical manufacturing: from batch to continuous production, J. Pharm. Innov. 10 (2015) 191–199.

[2] FDA, U.S. Department of Health and Human Services, Food and Drug Administration, Center for Drug Evaluation and Research (CDER), Quality Considerations for Continuous Manufacturing Guidance for Industry (Draft Guidence), 2019.

[3] The international conference on harmonization of technical requirements for registration of pharmaceuticals for human use (ICH), Quality Guideline Q8 Pharmaceutical Development, 2009.

[4] FDA, U.S. Department of Health and Human Services, Food and Drug Administration. Guidance for Industry: PAT – A framework for innovative pharmaceutical development, manufacturing, and quality assurance. 2004, 2004.

[5] J. Rantanen, J. Khinast, The future of pharmaceutical manufacturing sciences, J. Pharm. Sci. 104 (2015) 3612–3638.

[6] J. Djuris, Z. Djuric, Modeling in the quality by design environment: Regulatory requirements and recommendations for design space and control strategy appointment, Int. J. Pharm. 533 (2017) 346–356.

[7] K.V. Gernaey, R. Gani, A model-based systems approach to pharmaceutical product-process design and analysis, Chem. Eng. Sci. 65 (2010) 5757–5769.

[8] A. Saltelli, M. Ratto, T. Andres, F. Campolongo, J. Cariboni, D. Gatelli, M. Saisana, S. Tarantola, Global sensitivity analysis: the primer, John Wiley & Sons, 2008.

[9] M. Dosta, J.D. Litster, S. Heinrich, Flowsheet simulation of solids processes: current status and future trends, Adv. Powder Technol. 31 (2020) 947–953.

[10] R.M.C. Portela, C. Varsakelis, A. Richelle, N. Giannelos, J. Pence, S. Dessoy, M. von Stosch, When is an in silico representation a digital twin? a biopharmaceutical industry approach to the digital twin concept, Springer Berlin Heidelberg, Berlin, Heidelberg, pp. 1-21.

[11] Process Systems Enterprise, gPROMS, www.psenterprise.com/products/gproms, 1997-2020.

[12] F.C.C. Montes, K. Gernaey, G. Sin, Dynamic plantwide modeling, uncertainty, and sensitivity analysis of a pharmaceutical upstream synthesis: ibuprofen case study, Ind. Eng. Chem. Res. 57 (2018) 10026–10037.

[13] S. Diab, D.I. Gerogiorgis, Process modelling, simulation and technoeconomic evaluation of crystallisation antisolvents for the continuous pharmaceutical manufacturing of rufinamide, Comput. Chem. Eng. 111 (2018) 102–114.

[14] S. Diab, D.T. McQuade, B.F. Gupton, D.I. Gerogiorgis, Process design and optimization for the continuous manufacturing of nevirapine, an active pharmaceutical ingredient for HIV treatment, Org. Process Res. Dev. 23 (2019) 320–333.

[15] E. Içten, A.J. Maloney, M.G. Beaver, D.E. Shen, X. Zhu, L.R. Graham, J.A. Robinson, S. Huggins, A. Allian, R. Hart, S.D. Walker, P. Rolandi, R.D. Braatz, A virtual plant for integrated continuous manufacturing of a carfilzomib drug substance intermediate, part 1: CDI-promoted amide bond formation, Org. Process Res. Dev. (2020).

[16] E. Içten, A.J. Maloney, M.G. Beaver, X. Zhu, D.E. Shen, J.A. Robinson, A.T. Parsons, A. Allian, S. Huggins, R. Hart, P. Rolandi, S.D. Walker, R.D. Braatz, A virtual plant

for integrated continuous manufacturing of a carfilzomib drug substance intermediate, part 2: enone synthesis via a barbier-type grignard process, Org. Process Res. Dev. (2020).
[17] A.J. Maloney, E. Içten, G. Capellades, M.G. Beaver, X. Zhu, L.R. Graham, D. B. Brown, D.J. Griffin, R. Sangodkar, A. Allian, S. Huggins, R. Hart, P. Rolandi, S. D. Walker, R.D. Braatz, A virtual plant for integrated continuous manufacturing of a carfilzomib drug substance intermediate, part 3: manganese-catalyzed asymmetric epoxidation, crystallization, and filtration, Org. Process Res. Dev. (2020).
[18] A.J. Rogers, C. Inamdar, M.G. Ierapetritou, An integrated approach to simulation of pharmaceutical processes for solid drug manufacture, Ind. Eng. Chem. Res. 53 (2014) 5128–5147.
[19] G. Tian, A. Koolivand, N.S. Arden, S. Lee, T.F. O'Connor, Quality risk assessment and mitigation of pharmaceutical continuous manufacturing using flowsheet modeling approach, Comput. Chem. Eng. 129 (2019), 106508.
[20] Z. Wang, M.S. Escotet-Espinoza, M. Ierapetritou, Process analysis and optimization of continuous pharmaceutical manufacturing using flowsheet models, Comput. Chem. Eng. 107 (2017) 77–91.
[21] F. Boukouvala, V. Niotis, R. Ramachandran, F.J. Muzzio, M.G. Ierapetritou, An integrated approach for dynamic flowsheet modeling and sensitivity analysis of a continuous tablet manufacturing process, Comput. Chem. Eng. 42 (2012) 30–47.
[22] N. Metta, M. Ghijs, E. Schäfer, A. Kumar, P. Cappuyns, I. Van Assche, R. Singh, R. Ramachandran, T. De Beer, M. Ierapetritou, I. Nopens, Dynamic flowsheet model development and sensitivity analysis of a continuous pharmaceutical tablet manufacturing process using the wet granulation route, Processes 7 (2019) 234.
[23] M. Sen, A. Chaudhury, R. Singh, J. John, R. Ramachandran, Multi-scale flowsheet simulation of an integrated continuous purification–downstream pharmaceutical manufacturing process, Int. J. Pharm. 445 (2013) 29–38.
[24] M. Sen, A. Rogers, R. Singh, A. Chaudhury, J. John, M.G. Ierapetritou, R. Ramachandran, Flowsheet optimization of an integrated continuous purification-processing pharmaceutical manufacturing operation, Chem. Eng. Sci. 102 (2013) 56–66.
[25] B. Benyahia, R. Lakerveld, P.I. Barton, A plant-wide dynamic model of a continuous pharmaceutical process, Ind. Eng. Chem. Res. 51 (2012) 15393–15412.
[26] J.B. Dressman, J. Krämer, Pharmaceutical dissolution testing, Taylor & Francis Boca Raton, FL, 2005.
[27] N. Zaborenko, Z. Shi, C.C. Corredor, B.M. Smith-Goettler, L. Zhang, A. Hermans, C. M. Neu, M.A. Alam, M.J. Cohen, X. Lu, L. Xiong, B.M. Zacour, First-principles and empirical approaches to predicting in vitro dissolution for pharmaceutical formulation and process development and for product release testing, The AAPS Journal 21 (2019) 32.
[28] A. Balogh, A. Domokos, B. Farkas, A. Farkas, Z. Rapi, D. Kiss, Z. Nyiri, Z. Eke, G. Szarka, R. Örkényi, B. Mátravölgyi, F. Faigl, G. Marosi, Z.K. Nagy, Continuous end-to-end production of solid drug dosage forms: coupling flow synthesis and formulation by electrospinning, Chem. Eng. J. 350 (2018) 290–299.
[29] K. Tacsi, H. Pataki, A. Domokos, B. Nagy, I. Csontos, I. Markovits, F. Farkas, Z. K. Nagy, G. Marosi, Direct processing of a flow reaction mixture using continuous mixed suspension mixed product removal crystallizer, Cryst. Growth Des. 20 (2020) 4433–4442.
[30] B. Nagy, B. Szilágyi, A. Domokos, K. Tacsi, H. Pataki, G. Marosi, Z.K. Nagy, Z. K. Nagy, Modeling of pharmaceutical filtration and continuous integrated crystallization-filtration processes, Chem. Eng. J. 127566 (2020).
[31] H.S. Fogler, Essentials of chemical reaction engineering: essenti chemica reactio engi, Pearson Education, 2010.
[32] N. Hansen, A. Ostermeier, Completely derandomized self-adaptation in evolution strategies, Evol. Comput. 9 (2001) 159–195.
[33] Z.K. Nagy, R.D. Braatz, Distributional uncertainty analysis using power series and polynomial chaos expansions, J. Process Control 17 (2007) 229–240.
[34] R. Gunawan, I. Fusman, R.D. Braatz, High resolution algorithms for multidimensional population balance equations, AIChE J. 50 (2004) 2738–2749.
[35] M. Voelker, M. Hammer, Dissolution and pharmacokinetics of a novel micronized aspirin formulation, Inflammopharmacology 20 (2012) 225–231.
[36] J.B. Dressman, A. Nair, B. Abrahamsson, D.M. Barends, D. Groot, S. Kopp, P. Langguth, J.E. Polli, V.P. Shah, M. Zimmer, Biowaiver monograph for immediate-release solid oral dosage forms: acetylsalicylic acid, J. Pharm. Sci. 101 (2012) 2653–2667.
[37] H. Bundgaard, Influence of an acetylsalicylic anhydride impurity on the rate of dissolution of acetylsalicylic acid, J. Pharm. Pharmacol. 26 (1974) 535–540.
[38] A.D. Bond, K.A. Solanko, S. Parsons, S. Redder, R. Boese, Single crystals of aspirin form II: crystallisation and stability, CrystEngComm 13 (2011) 399–401.
[39] N. Kubota, J.W. Mullin, A kinetic model for crystal growth from aqueous solution in the presence of impurity, J. Cryst. Growth 152 (1995) 203–208.
[40] N. Kubota, Effect of impurities on the growth kinetics of crystals, Cryst. Res. Technol. 36 (2001) 749–769.
[41] M.D. Morris, Factorial sampling plans for preliminary computational experiments, Technometrics 33 (1991) 161–174.
[42] F. Campolongo, A. Saltelli, J. Cariboni, From screening to quantitative sensitivity analysis. a unified approach, Computer Physics Communications 182 (2011) 978-988.
[43] F. Pianosi, F. Sarrazin, T. Wagener, A matlab toolbox for global sensitivity analysis, Environ. Modell. Software 70 (2015) 80–85.
[44] F. Pianosi, F. Sarrazin, T. Wagener, http://bristol.ac.uk/cabot/resources/safe-toolbox/ (Accessed: 2020. 07.02.).
[45] US Food and Drug Administration. Guidance for Industry, Dissolution Testing of Immediate Release Solid Oral Dosage Forms, 1997.